NKS-455
ISBN 978-87-7893-548-9

Barsebäck as a Research and Development Platform, Extraction and Analysis of Service-aged and Irradiated Reactor Pressure Vessel Material

Pål Efsing[1,4], Magnus Boåsen[1,5], Daniela Klein[1]

Pentii Arffman[2], Noora Hytönen[2], Sebastian Lindqvist[2]

Mattias Thuvander[3], Kristina Lindgren[3]

Jenny Roudén[4]

[1] Department of Solid Mechanics, Royal Institute of Technology (KTH), SE-10044 Stockholm Sweden
[2] VTT Technical Research Centre of Finland Ltd, PO Box 1000, FI-02044 VTT, Helsinki, Finland
[3] Chalmers University of Technology, Department of Physics, SE-41296, Göteborg, Sweden
[4] Ringhals AB, SE-43285 Väröbacka, Sweden
[5] Current address: Uddeholm Tooling AB, SE-68385 Hagfors, Sweden

February 2022

Abstract

As part of the NKS-R program, VTT, Chalmers University of Technology and KTH have extended the mechanical and microstructural testing in order to analyze the as-aged material properties of the retired reactor pressure vessel, RPV, from Barsebäck unit 2. The current phase included Impact testing of material from the reactor pressure vessel and microstructural characterization of the weld metal using LOM, SEM and APT. Due to the nature of the work, the NKS-project is connected to a number of adjacent activities, including support from the Finnish Nuclear Safety Program, the SAFIR-program, the Swedish Radiation Safety Authority SSM and Swedish Centre for Nuclear Technology, SKC and Energiforsk.

Key words

Low alloy steel, irradiation effects, fracture toughness, ductile to brittle transition temperature, constraint effects, high resolution microscopy, microstructural characterization

NKS-455
ISBN 978-87-7893-548-9
Electronic report, February 2022
NKS Secretariat
P.O. Box 49
DK - 4000 Roskilde, Denmark
Phone +45 4677 4041
www.nks.org
e-mail nks@nks.org

Barsebäck as a Research and Development Platform, Extraction and Analysis of Service-aged and Irradiated Reactor Pressure Vessel Material

Final Report from the NKS-R BREDA-RPV 2021 activity

(Contract: AFT/NKS-R(21)118/1)

Pål Efsing[1,4], Magnus Boåsen[1,5], Daniela Klein[1]
Pentii Arffman[2], Noora Hytönen[2], Sebastian Lindqvist[2]
Kristina Lindgren[3], Mattias Thuvander[3]
Jenny Roudén[4]

[1] Department of Engineering Mechanics – unit of Solid Mechanics, Royal Institute of Technology (KTH), SE-100 44 Stockholm Sweden
[2] VTT Technical Research Centre of Finland Ltd, PO Box 1000, FI-02044 VTT, Espoo, Finland
[3] Chalmers University of Technology, Department of Physics, SE-412 96, Göteborg, Sweden
[4] Ringhals AB, SE-43285 Väröbacka, Sweden
[5] Current address: Uddeholm Tooling AB, 683 85 Hagfors

Table of contents

	Page
1. Introduction/Background	3
2. Preliminary mechanical test matrix for the BREDA/BRUTE project	4
3. Mechanical properties of thermally aged RPV steel from Barsebäck unit 2	4
4. Microstructural analysis of weld metal	5
5. Microstructural assessment of aged material using Atom Probe Tomography (APT)	6
6. Conclusions	6
7. References	7
Appendices 1 and 2	

1. Introduction/Background

As part of the NKS-R program in 2021, VTT, Chalmers University of Technology, and KTH have extended the contribution to the understanding of ageing effects on Reactor pressure vessel steels outlined in the previous summary reports dating from 2016 to 2020 [Efsing et al. 2016, 2018, 2019, 2020] regarding extraction, mechanical and microstructural testing, and analysis of materials harvested from a retired reactor pressure vessel, RPV, from the former Barsebäck Nuclear Power Plant. The overall objective of the study, which is a collaboration between the Swedish and Finnish nuclear utilities, regulatory bodies and academic resources, is to increase the current knowledgebase on the correctness of the existing surveillance programs, as well as the influence of long time thermal ageing of materials used for large pressure vessels in the nuclear industry such as the RPV and Pressurizer, PRZ. In 2016, a baseline study of the mechanical properties of the used materials to prepare the basis for a test program to analyze the as-aged material properties of the RPV from Barsebäck unit 2 was performed. Further, the program regarding the extraction methodology and the actual materials harvesting was outlined and initial qualification of the methodologies performed. Baseline assessment of the mechanical properties, literature studies and gathering of background information to support the testing of actual harvested materials was also part of the original scope. The harvesting work has been fully financed by Ringhals AB, Forsmark Kraftgrupp AB and OKG AB as part of an umbrella project under the auspices of Energiforsk with Monika Adsten as the primary program manager. The work connects to the BRUTE program, currently in progress under the Finnish state SAFIR umbrella ending 2022.

Activities from 2018 to 2020 included planning and extraction of trepans from the RPV of Barsebäck 2, decontamination and preparation of these at Ringhals and shipping the samples to Finland. As a pre-study a number of archive materials, both identical to the actual RPV and other weldments produced with weld metal of the same requirements, were studied in order to establish beginning of life micros structural and mechanical properties. The first step in the actual testing was performed using material form the RPV head (RPVH). The objective here was to establish a credible basis for the effect of thermal ageing in the material. In 2020, mechanical and microstructural tests were initiated.

The initial results have shown that the impact tests and hardness measurements are confirmative to each other, supporting suggestions made by [Efsing et al 2014] with respect to assessment of the effect of irradiation on the tensile and fracture mechanical properties to utilize hardness as an indicator for future test extension. Further, the microstructural characterization of the samples was extended to include also the beltline weld and was partially reported.

The key deliverables during BREDA-RPV 2021 are the open publications on the microstructural assessment of material from the RPVH [Hytönen et al 2021] and the weakest link model development of the thermally aged material [Boåsen et al 2021].

Two internal workshops have been held, one in May and one in September, via web-cast, to summarize the results from the mechanical testing performed so far and to bring up discussions on the continued activities in the area. The latter was initiated by Energiforsk to ensure dissemination of the results in an effective manner. The results are summarized below. In March, Ulla Ehrnsten presented the project including an update on the results at the Finnish SAFIR-2022 seminar.

KTH has completed a complementary activity studied the possibilities to reliably produce shallow edge defects on the surface of samples for mechanical testing. This is part of a different study but will allow for a firm foundation for future work regarding structural integrity of real components and the effects of constraint on irradiated and thermally aged material.

2. Preliminary mechanical test matrix for the BREDA/BRUTE project

A report describing the proposed work scope for the testing of mechanical properties of the material harvested from Barsebäck unit 2 was developed in a draft version during 2018 and finalized in 2019. [Boåsen 2019]. The report was transmitted to NKS as part of the reporting 2018 [Efsing et al. 2019]. According to the proposal, it is suggested that the test matrix includes testing of miniature Compact Tension, C(T), and Single Edge Notch Bend, SE(B) specimens to evaluate ductile and cleavage fracture behaviour and the influence of constraint on the mechanical properties. In addition to this, the proposed testing will include Charpy-V impact test specimens, microstructural samples, hardness measurements and tensile test specimens to fully categorize the mechanical properties of the aged material.

The test matrix has since then been finalized by VTT and is described in the BRUTE Summary report for 2020 [Ehrnstén 2020]. The report also describes the verification work performed to qualify the new hot-cell laboratory of VTT for work in the area.

3. Mechanical properties of thermally and irradiation aged RPV steel from Barsebäck unit 2

VTT has previously determined the transition curve for the reactor pressure vessel head weld metal by performing impact tests on 23 specimens removed from the 1/4T depth from the inner surface of the two of the delivered trepans from the RPVH. Analyses of the test results included impact energy and crack arrest force transition curve determinations as well as correlation evaluation between impact energy and lateral expansion and shear fracture appearance. When compared to the baseline results, the results indicate that the shift in the transition temperature for the weld metal is insignificant due to thermal embrittlement (280°C for 28 years). The brittle to ductile transition temperature (DBTT) T_{41J} was -75°C, and equal to that of the unirradiated and unaged baseline data. The results thus show that 28 years of operation has not changed the DBTT due to thermal ageing. The tensile properties of the SAW weld metal from the RPVH have been determined at four different temperatures, i.e., room temperature, 125 °C, 288 °C and 300 °C and results are similar to those of the baseline results. The results from the impact toughness tests of the weld metal were confirmed in 2020 from fracture toughness testing using miniature C(T) specimens. These were cut from the tested impact toughness test specimens, and revealed similar T_0 values for the RPVH weld to that of the base line weld.

During 2021 trepan #6 (trepan #2 by Ringhals designations), extracted from the axial beltline weld seam W14, was characterised comprehensively at 1/4T depth. Tensile and Charpy impact tests imply that the material properties are better, and consequently the transition temperature lower than the as delivered baseline result in the beltline. Additionally, tensile tests indicate discontinuity beyond the yield region. This is a possible indication of dynamic strain aging.

Brittle fracture toughness “Master curve” tests confirm that the beltline weld material is inhomogeneous in nature. Similar to the RPVH material, a multimodal Master curve model is considered best to describe the material. The extent of the inhomogeneity is lesser in the beltline than in the RPVH, however. The lower confidence bound is subsequently higher, again implicating better material in the beltline than the RPVH.

KTH has continued the effort on a weakest link model for brittle fracture that uses state of the art Finite Element Modelling (FEM) to study the effect of constraint on thermally aged material. The main bulk of the work is reported in [Boåsen 2021]. The framework is used in an expansion work performed by Daniela Klein at KTH. Daniela started her work with simulations of the proposed Round Notch Bend, RNB, specimens addressing the wish to find a specimen that would fail by one of the two proposed mechanisms only. The tests are now conducted, but the SEM evaluation is still pending due to the limitations set by the pandemic situation. The plan was to do these in Finland with VTT. The investigation is necessary to know if the initiation mechanisms proposed by Boåsen in his thesis work was predicted correctly. The outcome of the effort will be reported in future progress reports. Additionally, Shuyue Wang has started a complimentary project at KTH, supported by SKC, Swedish Centre for Nuclear Technology, aiming at expanding the modelling framework into the ductile failure regime. Thus, two further students are included in the future work and networking.

Here it can also be noted that Magnus was awarded the Sigvard Eklund's Prize for best PhD thesis for 2021 at the annual SKC seminar in October 2021. This marks the second straight year a Ph. D. student funded by NKS with-in the BREDA-project is awarded this price since Kristina Lindgren, Chalmers was the recipient of the price in 2020.

The test matrix for the remainder of the project was determined. Circumferential weld seam W16 in the beltline will be investigated similarly as the axial weld seam W14 in the same region and W28 in the head region. Tensile tests are increased, in order to investigate possible dynamic strain aging observed during testing of the axial beltline weld seam. Otherwise investigations follow similar structure to the previous materials. Surveillance materials, as well as accelerated irradiation specimens take focus once testing of W16 is finished.

Along the research done on Barsebäck 2 materials, the test methodology at VTT was further developed in 2021. Reconstitution of new impact specimens in hot cells from previously tested specimen halves was validated. A new tool for splitting of specimens not split completely during testing was designed and installed. Polishing of irradiated samples for microstructural examinations was developed, as well as GD-OES measurement, among others. Multiple tools for in-cell usage with manipulators were introduced. All progress has further trained the staff at VTT for expedited and secure specimen handling, testing and examination.

4. Microstructural analysis of weld metal

So far, detailed fractographic and microstructural investigations were performed on the impact and toughness specimens from the RPVH weld metal. Initiation at secondary particles was observed with lower toughness values correlating to larger initiating particles. Both broken and debonded particles were observed. The investigations revealed also an effect of the microstructure on the toughness, being lower when initiation occurs in the re-heated microstructure compared to as-welded microstructure. A scientific paper on the results from the impact toughness specimens investigation is in press.

The microstructure of the weld metal in the belt-line weld has been examined with optical microscope, SEM and EBSD techniques. The structure is typical of high quality welds, but there are possible small differences between the RPVH and beltline materials. EBSD mappings illustrate several different types of ferrite formations expected in the multipass welds. Fracture surfaces of specimens have been investigated with SEM and EDS. Similar features are found in brittle impact and fracture toughness specimens. Typically, an inclusion is found as the initiator but differences between RPVH and beltline fracture initiation are observed. Further study of beltline inclusions is ongoing.

5. Microstructural assessment of aged material using Atom Probe Tomography (APT)

The earlier achieved atom probe tomography (APT) data of the beltline region of Barsebäck RPV was further analysed. No obvious clustering was observed, but when performing some statistical analysis of the distribution of atoms, there might be some deviations between reference material and irradiated Barsebäck material. The extent and what this could mean in terms of clustering will be investigated by further data investigation during the coming year.

The project on annealing and hardness measurements and correlation to APT measurements of the Ringhals RPV surveillance and materials test reactor irradiated weld metal was continued. This year, some more of the annealed specimen were sent to Chalmers for APT analysis. All the new and earlier results were then summed up and written into a manuscript, that was submitted before the end of 2021. The paper was accepted in February 2022.

In the end of 2020, Kristina Lindgren was awarded funding from Jacob Wallenbergs Foundation to spend on research within materials science. In October 2021, she presented at the yearly seminar for the awardees at Slottsviken, including some examples on RPV steels. Kristina also made an on-line guest lecture at VTT on the use of APT as an analysis tool at VTT in June 2021. Chalmers is also involved in an EU-funded program, ENTENTE, on RPV steels.

A side note is that Chalmers will get a new APT instrument during 2022. The instrument is called LEAP 6000 XR (from Cameca) and will be replacing the existing LEAP 3000 X HR (Imago Scientific Instruments).

6. Conclusions

Samples have been extracted from the RPV of Barsebäck Unit 2 and those from the RPV head included in this program has been shipped to VTT. Several mile-stones of the project were completed in 2021, i.e. the mechanical testing of the RPVH was reported, and work on the irradiated material from the belt line commenced.

The current state of the art regarding the influence of constraint on fracture properties have been summarized and reviewed with the objective to lay a firm foundation for the envisaged testing. A finite element analysis has been performed to support the forth coming mechanical testing using fracture mechanical test techniques.

Results from the mechanical testing is starting to become available thus allowing for initial assessments of the resulting changes in the properties. This work is foreseen to commence in the end of 2022 extending into 2023 with expanded collaboration between the executing partners and the industrial/regulatory partners.

7. References

Arffman P., Impact test results from B2 RPV head SAW weld metal, VTT Research Report VTT-R-00942-19, 2019, 47 pages

Boåsen M. et. al, Preliminary mechanical test matrix for the BREDA-BRUTE project, VTT Research Report VTT-R-06849-18, 2019, 24 pages

Boåsen M. et al, A weakest link model for multiple mechanism brittle fracture—Model development and application, In *J of the Mechanics and Physics of Solids*, vol. 147, 2021

Efsing P et al. 2016, Barsebäck as research and development platform, extraction and analysis of reactor pressure vessel material, Final report for the BREDA2016 activity, NKS-385

Efsing P et al., 2018 Barsebäck as research and development platform, extraction and analysis of reactor pressure vessel material, Final report for the BREDA2018 activity, NKS-418

Efsing P et al, 2019 Barsebäck as research and development platform, extraction and analysis of reactor pressure vessel material, Final report for the BREDA2019 activity, rev 1, NKS-431

Efsing P et al, 2020 Barsebäck as research and development platform, extraction and analysis of reactor pressure vessel material, Final report for the BREDA2020 activity, NKS-443

Efsing P et al, 2014 Flux Effects on Radiation Induced Aging Behavior of Low Alloy Steel Weld Material with High Nickel and Manganese Content, In ASTM-STP 1572, Effects of Radiation on Nuclear Material, ASTM, West Conshohocken, PA, USA, doi: 10.1520/STP157220130112

Ehrnstén et. al., Barsebäck reactor pressure vessel material used for true evaluation of embrittlement (BRUTE), 2020

Hytönen et al, Effect of weld microstructure on brittle fracture initiation in the thermally-aged boiling water reactor pressure vessel head weld metal, In *Int. Journal of Minerals, Metallurgy and Materials*, Volume 28, Number 5, May 2021

Acknowledgements

NKS conveys its gratitude to all organizations and persons who by means of financial support or contributions in kind have made the work presented in this report possible.

The support from the Finnish nuclear safety program, the SAFIR2022-program, the Swedish Radiation Safety Authority and the Swedish Centre for Nuclear Technology, SKC and finally the Swedish Nuclear Power Plants permit holders and owners (Ringhals AB, Forsmarks Kraftgrupp AB, OKG AB, Vattenfall AB and Uniper) for the work is gratefully acknowledged. Some of the adjacent work is part of a research program coordinated by Energiforsk with Monika Adsten as the program manager

Disclaimer

The views expressed in this document remain the responsibility of the author(s) and do not necessarily reflect those of NKS. In particular, neither NKS nor any other organization or body supporting NKS activities can be held responsible for the material presented in this report.

Appendices

1. N Hytönen et. al., Effect of weld microstructure on brittle fracture initiation in the thermally-aged boiling water reactor pressure vessel head weld metal, International Journal of Minerals, Metallurgy and Materials Volume 28, Number 5, May 2021, Page 867 https://doi.org/10.1007/s12613-020-2226-6.

2. M Boåsen et. al., A weakest link model for multiple mechanism brittle fracture - Model development and application, In *J of the Mechanics and Physics of Solids*, vol. 147, 2021

Bibliographic Data Sheet **NKS-455**

Title	Barsebäck as a Research and Development Platform, Extraction and Analysis of Service-aged and Irradiated Reactor Pressure Vessel Material

Author(s)	Pål Efsing[1,4], Magnus Boåsen[1,5], Daniela Klein[1] Pentii Arffman[2], Noora Hytönen[2], Sebastian Lindqvist[2] Mattias Thuvander[3], Kristina Lindgren[3] Jenny Roudén[4]
Affiliation(s)	[1] Department of Solid Mechanics, Royal Institute of Technology (KTH), SE-10044 Stockholm Sweden [2] VTT Technical Research Centre of Finland Ltd, PO Box 1000, FI-02044 VTT, Helsinki, Finland [3] Chalmers University of Technology, Department of Physics, SE-41296, Göteborg, Sweden [4] Ringhals AB, SE-43285 Väröbacka, Sweden [5] Current address: Uddeholm Tooling AB, 683 85 Hagfors

ISBN	978-87-7893-548-9
Date	February 2022
Project	NKS-R / BREDA2021 activity (Contract: NKS_R_2016_118)
No. of pages	8
No. of tables	0
No. of illustrations	0
No. of references	6

Abstract max. 2000 characters	As part of the NKS-R program, VTT, Chalmers University of Technology and KTH have extended the mechanical and microstructural testing in order to analyze the as-aged material properties of the retired reactor pressure vessel, RPV, from Barsebäck unit 2. The current phase included Impact testing of material from the reactor pressure vessel and microstructural characterization of the weld metal using LOM, SEM and APT. Due to the nature of the work, the NKS-project is connected to a number of adjacent activities, including support from the Finnish Nuclear Safety Program, the SAFIR-program, the Swedish Radiation Safety Authority SSM and Swedish Centre for Nuclear Technology, SKC and Energiforsk.

Key words	Low alloy steel, irradiation effects, fracture toughness, ductile to brittle transition temperature, constraint effects, high resolution microscopy, microstructural characterization

International Journal of Minerals, Metallurgy and Materials
Volume 28, Number 5, May 2021, Page 867
https://doi.org/10.1007/s12613-020-2226-6

Effect of weld microstructure on brittle fracture initiation in the thermally-aged boiling water reactor pressure vessel head weld metal

Noora Hytönen[1)], *Zai-qing Que*[1)], *Pentti Arffman*[1)], *Jari Lydman*[1)], *Pekka Nevasmaa*[1)], *Ulla Ehrnstén*[1)], *and Pål Efsing*[2)]

1) Nuclear Reactor Materials, VTT Technical Research Centre of Finland Ltd., Kivimiehentie 3, P.O. Box 1000, FI-02044 VTT, Finland
2) Department of Solid Mechanics, Royal Institute of Technology (KTH), SE-100 44 Stockholm, Sweden

(Received: 9 September 2020; revised: 20 October 2020; accepted: 18 November 2020)

Abstract: Effects of the weld microstructure and inclusions on brittle fracture initiation are investigated in a thermally aged ferritic high-nickel weld of a reactor pressure vessel head from a decommissioned nuclear power plant. As-welded and reheated regions mainly consist of acicular and polygonal ferrite, respectively. Fractographic examination of Charpy V-notch impact toughness specimens reveals large inclusions (0.5–2.5 μm) at the brittle fracture primary initiation sites. High impact energies were measured for the specimens in which brittle fracture was initiated from a small inclusion or an inclusion away from the V-notch. The density, geometry, and chemical composition of the primary initiation inclusions were investigated. A brittle fracture crack initiates as a microcrack either within the multiphase oxide inclusions or from the debonded interfaces between the uncracked inclusions and weld metal matrix. Primary fracture sites can be determined in all the specimens tested in the lower part of the transition curve at and below the 41-J reference impact toughness energy but not above the mentioned value because of the changes in the fracture mechanism and resulting changes in the fracture appearance.

Keywords: reactor pressure vessel; brittle fracture; weld microstructure; thermal aging

1. Introduction

Structural integrity of the reactor pressure vessel (RPV) in a nuclear power plant is of utmost importance. During operation, the RPV is subjected to thermal loading and neutron irradiation, which can cause embrittlement and shift the ductile-to-brittle transition temperature (DBTT) of ferritic steel weld with a body-centered cubic crystal structure toward high temperatures [1]. Embrittlement is monitored using surveillance programs, which state and predict the embrittlement and ensure safe margins toward brittle fracture. These programs use either Charpy V-notch (CVN) impact and/or fracture toughness test specimens. Welds are typically more critical than base materials in terms of irradiation-induced embrittlement. Embrittlement of RPV steels and weld metals is extensively studied [2–8], and numerous investigations are ongoing.

Understanding the microstructural factors affecting brittle fracture initiation and how they may be influenced by thermal aging and/or irradiation is important to achieve the improved mechanistic comprehension of brittle fracture and embrittlement. The first theories about the brittle fracture initiation mechanism were introduced by Griffith [9]. In this classical description of the problem, a microcrack is assumed to initiate within a brittle particle when the stress exceeds a critical value. The microcrack propagates from the broken particle and develops into a macrocrack. However, microcracks can also be initiated at the interface between secondary particles and matrixes because of debonding [10]. Nevertheless, stress concentration in a particle is always greater than that at the interface [10]. The weakest link model for crack initiation at a particle was introduced first by Weibull [11–12] and later modified by Beremin *et al.* [13]. The abovementioned models describe the relationship between a particle size and probability for brittle fracture initiation [2,14–17]. Bowen *et al.* [18] concluded that carbides in a martensitic base material are primary initiators of brittle fracture. Hein *et al.* [19] noted a difference between RPV base materials and weld metals, in which inclusions were the primary initiators. Investigations into thermally-aged weld metals and steels at high temperatures have concluded that thermal aging changes the initiation of brittle fracture from

Corresponding author: Zai-qing Que E-mail:Zaiqing.Que@vtt.fi

particles to intergranular (IG) fracture [20–21]. Thus, extensive data on the role of microstructure on brittle fracture initiation is needed and should be used in further developing brittle fracture models [20].

Weld metals contain secondary particles of different types and sizes. Nickel (Ni), manganese (Mn), and silicon (Si) form complex inclusions that promote the formation of acicular ferrite. Acicular ferrite is the desired weld microstructure resulting in good toughness properties [22–24]. However, RPV operating conditions are known to promote brittleness due to increased clustering and embrittlement during irradiation [3–4,25–26]. Thermal aging of a high-Ni-content weld metal in a pressurizer at 350°C for 27 years has been observed to cause an increase in the DBTT [3] and clustering [27] and the initiation of low toughness fracture as IG fracture. Single-phase inclusions such as simple oxides and sulfides (Al_2O_3, MnO, and MnS) cannot nucleate acicular ferrite. Nucleation on an inert surface is a heterogeneous process in which interfacial energy is a major controlling factor [28]. Hence, complex multiphase inclusions are highly effective nucleation sites [24]. Furthermore, the mechanism for acicular ferrite nucleation is dependent on the surface area of the inclusions, and thus, intermediate-sized inclusions or small inclusions on a high density promote acicular ferrite nucleation effectively [29]. Oxide inclusions, treated as brittle particles that fulfill the Griffith criterion of brittle fracture initiation, may act brittle because of the intrinsic crystal structure or the preceding small defects within the inclusions that are likely to initiate cleavage fracture. For oxysulfides, which are highly ductile, matrix debonding can induce cracking within materials and cause further fracture. The characterization of inclusions of investigated weld metal is essential for understanding brittle fracture initiation mechanisms [30].

The investigated RPV weld metal is from a decommissioned boiling water reactor, which had been operated for 23 effective full power years at 288°C. The investigated weld metal is high in Ni and Mn. The same weld metal is used in several reactors, and it has been investigated earlier e.g., using surveillance materials [4,20,31–32]. The current investigation is part of larger programs, namely, BREDA and BRUTE. It involves mechanical testing and microstructural characterization on RPV head and beltline materials. The main objective of the project is to verify surveillance results by using RPV materials from a decommissioned nuclear power plant and to gain rich mechanistic insights. Meanwhile, the current study aims to broaden the understanding of the factors affecting brittle fracture by characterizing the weld metal of an RPV head removed from a decommissioned RPV subjected to thermal aging but not to irradiation. The characterization focuses on the microstructure, CVN brittle fracture initiation, and primary fracture inclusion initiators.

2. Experimental

The material investigated herein was from the decommissioned Barsebäck Unit 2 boiling water reactor. The reactor was in operation for 23 effective full power years at 288°C. Cylinder-shaped trepans were drilled from the RPV head weld and used for mechanical tests and microstructural characterization. The investigated weld metal was manufactured using the submerged arc welding (SAW) method while the remaining ~16 mm- of the ~70-mm-thick weld was made using manual metal arc (MMA) welding. The trepans were machined into smaller sections and plates, from which the investigated specimens were cut. The investigated filler materials, namely, Phoenix-Union S3NiMo in the SAW weld and Oerlicon Tenacito 65 in the MMA weld, were high in Ni and Mn. The chemical composition of the weld based on optical emission spectrometry is presented in Table 1. The yield strength and tensile strength are 520 and 610 MPa, respectively.

Table 1. Chemical composition of weld metal according to optical emission spectrometry wt%

Weld	C	Mn	Ni	Si	Mo	Cr	S	P	Cu	Al	Ti	Co
SAW weld	0.057	1.43	1.48	0.15	0.41	0.03	0.007	0.008	0.060	0.024	0.003	0.020
MMA weld	0.037	1.38	1.22	0.25	0.37	0.03	0.007	0.007	0.004	0.002	0.004	0.018

2.1. Optical microscopy

The weld solidification microstructure, heat-affected zone (HAZ), and base material were characterized using the Zeiss Axio Observer 7 inverted optical microscope to observe and distinguish the different phases and microstructural features. The metallography specimens were polished and etched with 3vol% Nital solution (HNO_3 + ethanol). The multipass weld microstructure was examined through the wall thickness and involved samples from the inner wall side welded with the SAW method and the outer wall side welded with the MMA welding method (Fig. 1). Macro- and micro-hardness measurements (HV_{10}, HV_1) were performed to establish the relation between microstructure and hardness.

The location of the investigated microstructure, i.e., as-welded or reheated region, was determined from cross sections prepared as close as possible to the initiation site after the fractography.

2.2. Inclusion analysis

Using the Genesis Software, the density, geometry, and chemical composition of inclusions in the SAW weld microstructure was investigated through energy dispersive X-ray spectroscopy (EDS) with 10 keV at a current density of 3 nA. An automated feature-sizing analysis was used for the size

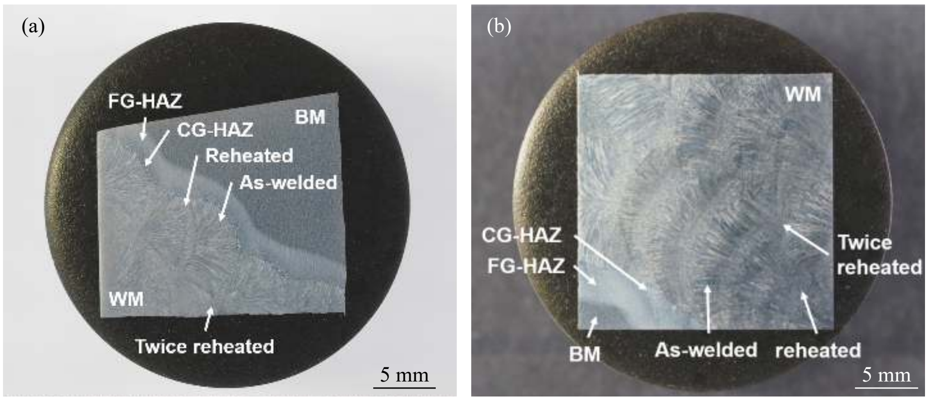

Fig. 1. Specimens for the characterization of investigated weld: (a) specimen from the inner wall side welded by the SAW method; (b) specimen from the outer wall side welded by the MMA welding method. Different metallurgical regions are indicated using arrows, i.e., base material (BM), weld metal (WM), fine-grained (FG), and coarse-grained (CG) HAZ.

distribution as the inclusions were recognized automatically through preset thresholds in the image brightness histogram. Statistical chemical analysis was performed using Genesis Chem, in which point analysis was automatically performed from the centroid of each recognized particle.

The inclusion analysis for the as-welded and reheated regions was conducted with an imaging field covering an area of 75 μm × 57 μm on an image with a resolution of 2048 px, resulting in a pixel size of 35 nm. As 2 px is the minimum size for features to be recognized as an inclusion, a sufficiently identified minimum inclusion size is 70 nm. In this work, 1339 inclusions (from eight fields) and 960 inclusions (from nine fields) were analyzed for the as-welded and reheated zones, respectively.

The analysis of the potential primary brittle fracture inclusions with large sizes (>0.35 μm) was conducted with an imaging field covering an area of 217.4 μm × 169.8 μm on an image with a resolution of 2048 px, resulting in a pixel size of 106 nm. A total of 100 fields were examined, and 9398 inclusions were analyzed with a total scanned area of 3.69 mm^2.

2.3. Charpy V-notch impact toughness testing

The CVN impact toughness specimens were tested according to the standard SFS-EN ISO-148-1:2016 [33]. The tests were performed using a Zwick RKP450 instrumented pendulum with automatic temperature control and feeding system. The pendulum was equipped with a 2-mm striker with a nominal impact energy of 300 J. Instrumented strain gauges in the striker tip measured the impact force and was compared with deflection in terms of the pendulum angle. The frictional loss measured regularly for free swings and estimated individually for each test consistently yielded a loss of 1.0–1.3 J.

The standard specimens measured 55 mm × 10 mm × 10 mm. The specimens for the CVN impact toughness test were cut at one-quarter from the inner surface, with the notch in the middle of the weld. The orientation of the CVN specimens was T-S, which is different from the recommended T-L orientation [34]. In the weld structure, L is the longitudinal direction of welding around the RPV while S is the building direction of the multipass weld.

The transition curve was formed by the transition temperature reference points determined at impact toughness energies of 28, 41, and 68 J on a tanh curve with a low shelf impact energy conservatively set to 2 J and an upper shelf estimated as the mean of completely ductile tests. The first test was performed at ambient temperature, and the subsequent temperatures were selected according to the development of the transition curve.

2.4. Fractographic examination

The fracture surfaces of nine CVN specimens with brittle-like fracture appearance from the lower shelf of the transition curve were investigated using the scanning electron microscope Zeiss Crossbeam 540. The characterization focused on the primary fracture initiation sites and their surrounding areas. The distance of the initiation location was measured from the V-notch to further evaluate the triaxial stress state.

The aim of the analysis was to identify the features and local chemical composition differences at or adjacent to the fracture initiation sites that exerted an impact on fracture behavior. The semiquantitative chemical compositions of the primary fracture area and initiation site were obtained using EDAX Octane Plus EDS. The topography of the fracture surface inevitably affects EDS mapping. Herein, the semiquantitative results revealed the different compositions of the particles relative to the surrounding weld and could thus be compared with the results of the inclusion analysis.

3. Results

3.1. Microstructure

The multipass weld is built by weld beads with average heights of 4 and 3 mm in the weld parts from SAW and

MMA welding, respectively, with reheated regions measuring approximately 1 mm in height. The HAZ is uniform throughout the weld and can be divided into fine-grained (FG) and coarse-grained (CG) regions. The weld microstructure is shown in Fig. 2. The epitaxial grain growth begins from the CG-HAZ across the fusion line in the preferred crystallographic direction <100> and inwards to the weld (Fig. 2(a)). The acicular ferrite forms into the parent austenite grains during the solidification of the weld bead. Most of the dendritic weld beads consist of intragranularly nucleated acicular ferrite with small fractions of grain boundary ferrite between the dendrites (Fig. 2(b)). Acicular ferrite has a typical fine basket weave structure and differs significantly from the pre-eutectoid grain boundary ferrite observed as light-colored elongated areas.

In multipass welding, the heat input from consecutive layers affects the microstructure of the as-welded grain structure by refining the dendritic grains through recrystallization. The reheated microstructure aligns the fan-shaped weld bead of the new weld layer. The reheated microstructure is shown in Fig. 2(c), where the microstructure mainly consists of polygonal ferrite. Polygonal ferrite appears as light-colored areas in the microstructure without a particular shape. The SAW and MMA welds show no significant differences in microstructure. Only a few large TiC particles are observed in the MMA weld, and they may be due to the impurities from the welding process. In the MMA HAZ region, a few grains of martensite are observed.

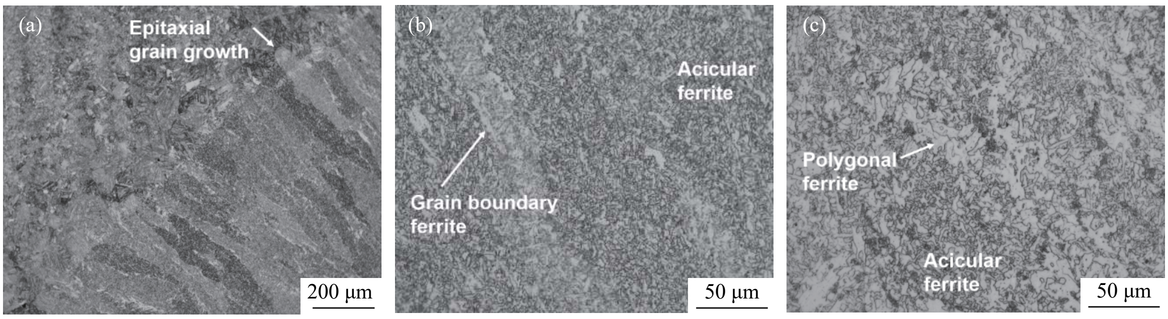

Fig. 2. Regions of weld microstructure: (a) epitaxial growth over the fusion boundary from the parent grain in the CG-HAZ toward the weld solidification bead; (b) weld bead microstructure with acicular ferrite and grain boundary ferrite; (c) reheated microstructure containing mainly polygonal ferrite.

The Vickers hardness results measured on 98.1-N load across the weld build-up thickness from the inner wall to the outer wall are shown in Fig. 3, which highlights an average hardness of HV_{10} 210 ± 5. The lower hardness of up to 12 mm from the inner wall is due to the thermal effect from the cladding process. The plots do not indicate differences between the two welding methods. HV_1 is measured over the fusion line, indicating the highest hardness peak at the CG-HAZ region. According to the hardness measurements, i.e., HV_{10} and HV_1, no large areas show a hardened microstructure because the size of the martensitic grains is smaller than that of the indents.

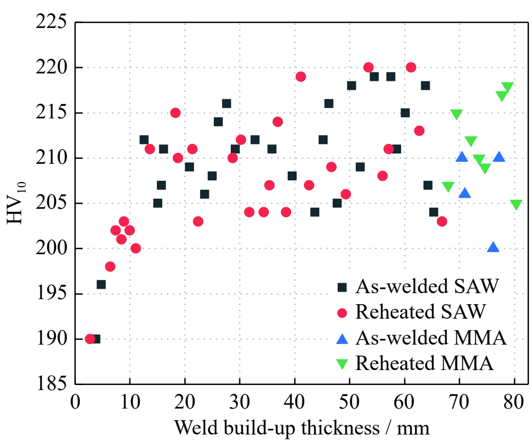

Fig. 3. HV_{10} results based on wall thickness. The results are divided into as-welded and reheated regions with SAW or MMA welding methods; the build-up thickness is measured from the inner wall to outer wall.

3.2. Inclusion analysis

The secondary particles in the as-welded and reheated microstructural regions are investigated separately on the metallography specimens. The analyses include the inclusion distribution and geometry analysis (size, aspect ratio, area, and diameter). Table 2 presents the average diameter and density of the inclusions for the as-welded and reheated regions. With regard to the inclusion density, the as-welded region has approximately 1.5 times more inclusions than the reheated

Table 2. Average inclusion size and density in as-welded and reheated microstructures

Region	Average diameter / μm	Density / mm^{-2}
As-welded	0.288	40805
Reheated	0.325	25995

region. The average size is slightly smaller in the as-welded region (0.288 μm) than in the reheated microstructure (0.325 μm). Statistically, the most probable inclusion sizes are 0.23 μm in the as-welded region and 0.27 μm in the reheated region (Fig. 4(a)). The aspect ratio of all the measured inclusions is close to 1, indicating that the inclusions are mostly spherical as expected.

The analysis of the potential primary brittle fracture initiators with large sizes (0.35–5 μm) reveals 9398 inclusions in a total scanned area of 3.69 mm^2, resulting in an inclusion density of 2546 mm^{-2}. The inclusion density with the inclusion diameters of the potential primary brittle fracture inclusions is shown in Fig. 4(b). The smallest and biggest inclusions recorded herein have diameters of 0.32 and 4.69 μm, respectively. However, only three inclusions have diameters larger than 1.8 μm in the scanned area. The inclusion density of the potential primary brittle fracture inclusions is more reasonable than the average results from the as-welded and reheated regions shown in Fig. 4(a) (the accumulated density of particles with diameters above 0.4 μm).

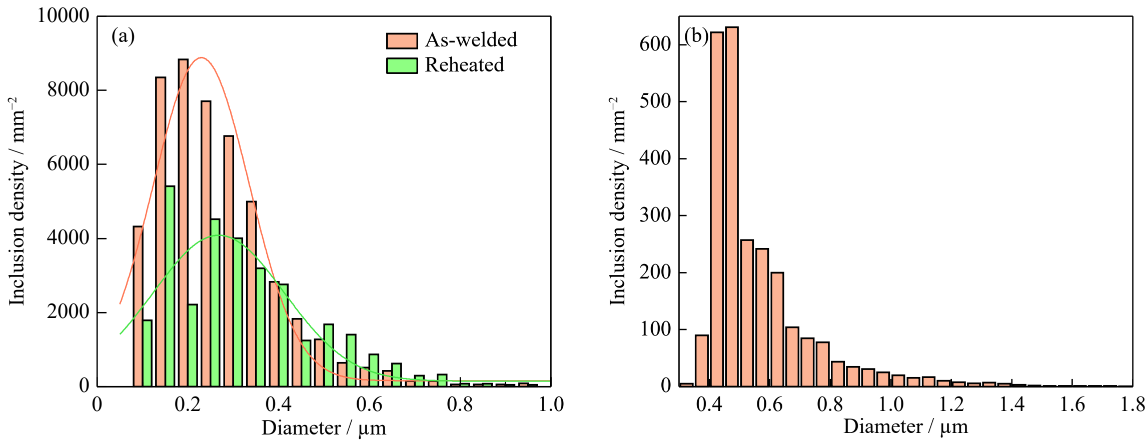

Fig. 4. (a) Inclusion density with inclusion diameters in the as-welded and reheated regions following the log-normal fitting; (b) inclusion density with inclusion diameters for the potential primary brittle fracture initiators in weld metal.

The chemical analyses are conducted with the electron beam set at 10 keV, which produces an interaction volume with a diameter of about 400 nm on Fe (based on a Monte Carlo simulation and comparable to the detected inclusion size). Limited background signals from the matrix materials are collected, and they lead to a reasonably precise chemical composition analysis. The average chemical composition of the 9398 large inclusions in weld metal is listed in Table 3. The main elements detected are Fe, Mn, Al, Si, O, and S. In Fig. 5, the main elements are given in ternary diagrams of Mn–Si–Al and S–Fe–O. The element content of the inclusion is higher when the circle is closer to the corner, and the size of the circle corresponds to the size of the inclusion. The color of the circle is a mix of RGB colors and varies with the

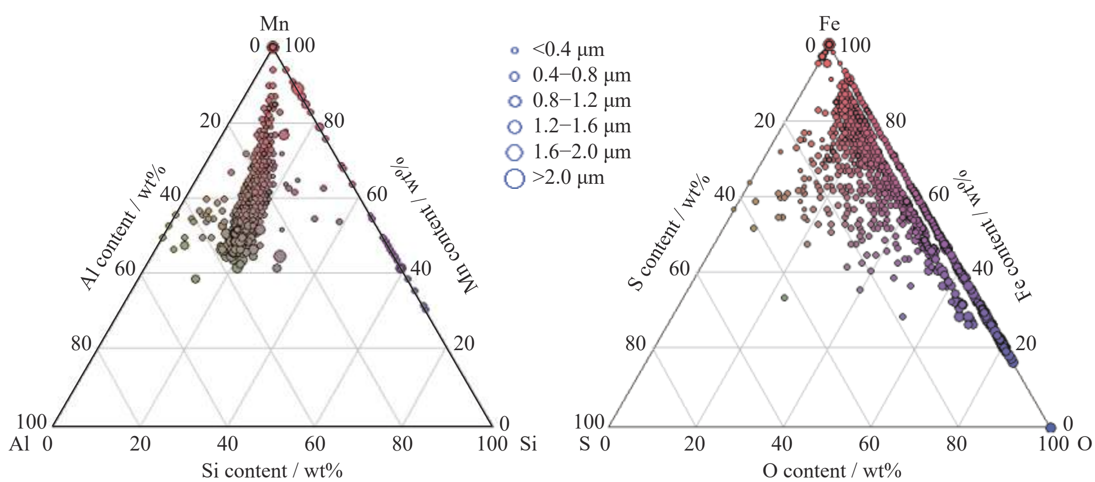

Fig. 5. Ternary diagrams of major elements (Mn–Al–Si and S–Fe–O) and size correlations for the potential primary brittle fracture inclusions—the analysis is conducted using large inclusion particles; the size scale is presented in the middle.

concentration of the corner elements. The inclusions in the weld metal are mainly Fe–Mn–Al-containing (S)O complex compounds, which consist of mixing oxides (Al, Si, Fe, and Mn oxides) and sulfides (Mn and Fe sulfides). The size of the inclusions increases with the O and/or Fe content. A limited amount of pure oxides or sulfides exist, but the amount of pure oxides is at least a magnitude higher than that of the pure sulfide inclusions.

Table 3. Average chemical composition of potential primary brittle fracture inclusions with large sizes (0.35–5 μm) in weld metals wt%

Fe	Mn	Al	Si	O	S
38.02	25.75	11.93	7.26	15.55	1.49

3.3. Fractography

The transition curve in the project is formed by 23 CVN specimens from a one-quarter depth of the trepans. Among the CVN specimens, nine from the lower shelf are included in the fractographic investigation. The fractography results indicate that the 41-J reference point seems to be the location where the brittle fracture mechanism changes as the specimens tested above that impact energy do not present a determinable primary fracture site, whereas all the specimens tested at and below 41 J reflected such sites. Fig. 6 shows the full transition curve obtained in the testing. The investigated brittle specimens are from the lower part of the transition curve indicated in the figure.

The reference transition temperatures obtained in the CVN impact toughness testing are $T_{28J} = -85°C$, $T_{41J} = -75°C$, and $T_{68J} = -60°C$, with the uncertainty estimated to be ±5°C. These values are similar to those of the non-aged reference material, thus indicating the negligible thermal embrittlement effect. The specimens included in the fractographic investigations are those tested below the transition temperature of $T_{41J} = -75°C$ [35].

In the fracture surface characterization, the brittle fracture initiated in all specimens by transgranular fracture and an inclusion is found at the initiation site in each specimen. An example of a brittle fracture surface is shown in Fig. 7(a), in which the initiation site is marked with a red square. The cleavage fracture can be determined according to the characteristic river patterns. In the fractographic examination, both mating fracture surfaces are investigated as the inclusion or part of it may remain on the halves. Fig. 7(b) shows the magnified primary initiation site showing an inclusion. In most of the investigated fracture surfaces, relatively large uncracked inclusions measuring 1.5–2.5 μm exist at the initiation site.

Interdendritic (ID)-like and IG-like fracture areas as the secondary fracture mode in addition to cleavage fracture are observed in some of the as-welded and reheated microstructures, respectively. The ID-like fracture surface shown in Fig. 8 has presumably propagated along the grain boundary ferrite. This phenomenon has also been observed in the reference state, i.e., in the non-aged state of the same material. The fracture is not considered to be brittle as small dimples and flakes are observed at the ID/IG-like areas. However, the topography imitates the underlying microstructure in these areas. All initiation sites are located in the as-welded microstructure; they are not found in the reheated microstructure.

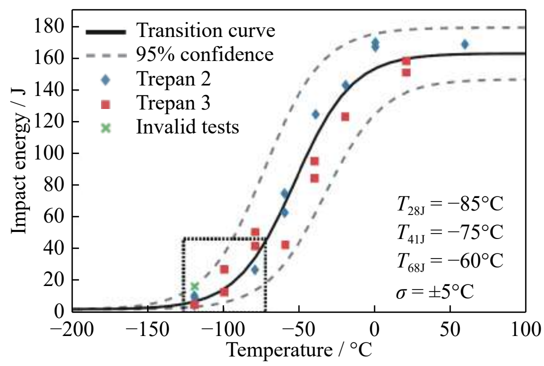

Fig. 6. Transition curve of Charpy V-notch impact toughness specimens.The investigated specimens with brittle fracture are inside the square.

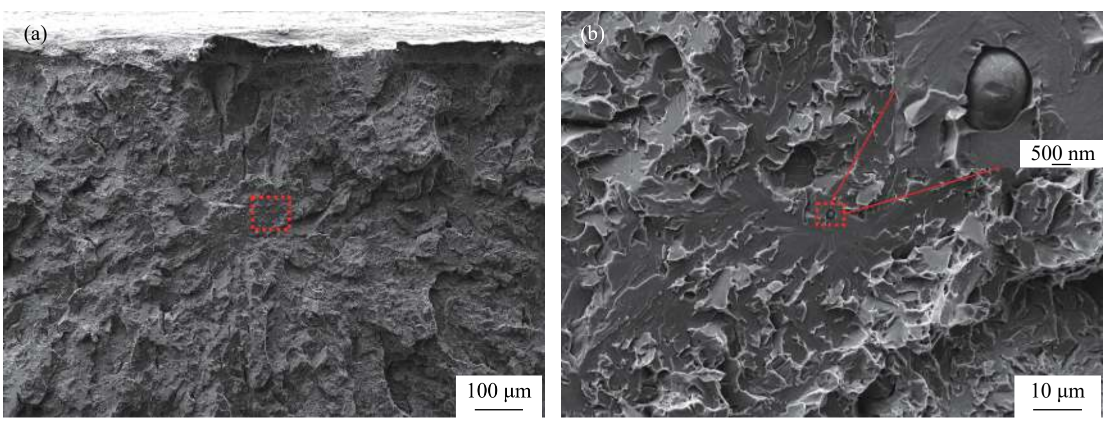

Fig. 7. Brittle cleavage fracture surface and an inclusion at the primary initiation site: (a) brittle cleavage fracture surface; (b) an inclusion at the primary initiation site.

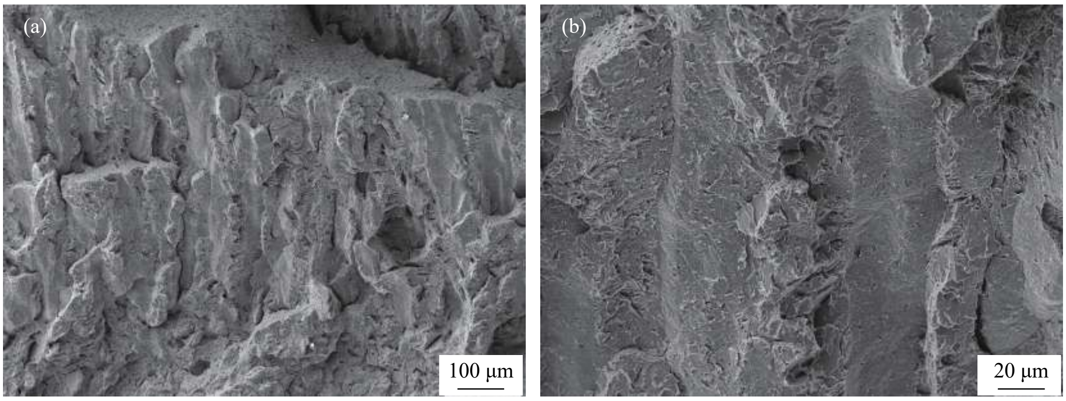

Fig. 8. (a) Interdendritic-like fracture in the as-welded region and (b) its higher magnification image. The fracture surface is not fully brittle.

This result is evidently due to the location of the notch in the weld bead.

4. Discussion

The presence of inclusions exerts an effect on brittle cleavage crack initiation [29]. Weld metals are composed of numerous and rather evenly distributed granular inclusions and are thus different from the base materials, in which the inclusions are typically large and sparsely distributed. The probability of an inclusion with suitable size for brittle fracture initiation is thus much higher in weld metals than in base materials, in which carbides become the weakest link [18]. The weld bead microstructure mainly contains acicular ferrite and polygonal ferrite, with the former having greater toughness properties. During solidification, the grain boundary ferrite nucleates first at the austenite grain boundaries while the acicular ferrite nucleates at the surface of the nonmetallic inclusions [36]. Widmanstätten ferrite may form at the parent austenite grain boundaries in competition with acicular ferrite. Alloying elements, such as Mn, promote the growth of acicular ferrite over the grain boundary phases [23]. No significant amount of Widmanstätten ferrite with lath structure was observed because of sufficient alloying and welding parameters. All initiation sites in the investigated specimens with brittle fractures are located in the as-welded microstructure. The large number of inclusions with large sizes (0.5–2.5 μm) in the reheated region are shown in Fig. 4(b), and the large particles are normally predicted to be the brittle fracture initiators. However, the as-welded region with a dendritic microstructure can increase the probability of brittle fracture initiation relative to the reheated region with a granular microstructure and short crack paths. Further investigations are required to verify the superiority of the influence of the dendritic as-welded microstructure and large multiphase inclusions on brittle fracture initiation.

The correlation between the primary initiation particle parameters, namely, size and location, and the CVN impact energy of less than 41 J is grouped by testing temperature and plotted in Fig. 9. The specimens with large initiator particles result in relatively low-value impact toughness energies when tested at the same temperature (Fig. 9(a)). The large

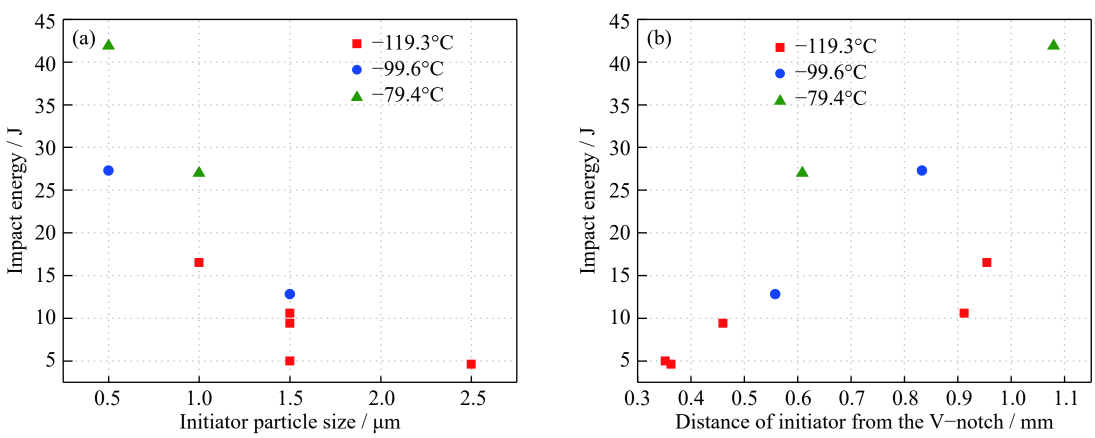

Fig. 9. Relation between primary initiation particle size (μm) (a) and distance of the initiator from the V-notch (mm) (b) with impact energy. The specimens tested in the lower part of the transition curve show a trend as the weakest location in the process zone of the testing temperature breaks first.

particle size (1.5–2.5 μm) is correlated with the impact toughness energy below 15 J. For large particles, the required applied stress to separate the interfaces is relatively low because the energy release rate increases with the particle size for the same applied stress [28]. The preceding plastic deformation and ductile region before the brittle fracture region in the CVN specimens are small at low values of impact energies. Therefore, the primary initiation site is also closer to the V-notch at a low impact toughness energy (Fig. 9(b)). The inclusion density and size distribution in the studied material show that the brittle fracture tends to initiate from the largest particle in the effective process zone acting as the weakest location and thus fulfills the weakest link theory. Nevertheless, a CVN specimen tested at −59.8°C with an impact toughness energy of 62.9 J from the transition region of the DBTT curve has multiple initiation sites, with the primary initiation site being undetectable, in the relative adjacency of the V-notch. Additionally, the initiation particle parameters with impact energy do not fit the current trend, thereby demonstrating that the correlation is only fulfilled with the specimens tested below 41 J in the lower part of the transition curve.

Particle interface debonding is observed in the specimens in the lower part of the transition curve, where the plastic flow is limited. In Fig. 7(b), a debonded inclusion is shown at a cleavage fracture initiation site. Debonding is normally associated with void nucleation during plastic deformation when a second-phase particle remains more or less intact. The plastic strain breaks the interatomic bonding between the matrix and the particle instead of breaking the inclusion. The large inclusions increase the local inhomogeneity, which then promotes debonding. The interface debonding may initiate a microcrack in the surrounding brittle material and propagate as a macroscale cleavage fracture at low temperatures. Depending on the particle size, temperature, and chemical composition of the inclusion and the stress state, the microcrack initiates inside the inclusion or at the interface between the inclusion and the weld metal matrix [1,8–9,17,30,37–38]. Hence, multiple active mechanisms are needed to explain the behavior for aged materials because the traditional methodology, i.e., Griffith's theory with failure of an inclusion, is not enough without parallel mechanisms, such as the debonding of particles and/or grain boundary. In the model developed by Boåsen [20], debonding resulting from thermal aging is observed under high temperatures. The debonding may also be due to the segregation of impurities on the particle surfaces and reduction of the interface adhesion, because the effect of thermal embrittlement was not observed in the impact toughness of the investigated weld material. The chemical composition inhomogeneity and weak bonding at the interfaces are the probable causes of debonding on which thermal aging may have an effect. In addition to particle debonding, ID- and IG-like failures are observed. These phenomena are related as they result from the breaking of interfaces. As the low-temperature toughness properties increase, the relatively high-Ni-content (1.4wt%–2.5wt%) in the weld metal increases the amount of grain boundary impurity segregation, which then seems to promote the ID/IG-like fracture mode [3,14]. Moreover, similar but brittle fracture areas are detected in the specimens with thermal aging-induced embrittlement, and the amount of ID/IG fracture is associated with the extent of DBTT shift [3]. The ID/IG fracture areas of brittle RPV welds are related to solute segregation, most commonly phosphorus [21,25,39].

According to the semiquantitative EDS analysis of the primary initiation sites, the particles at the crack initiation sites are mostly multiphase oxides. The main detected elements are Mn, Si, and Al, all of which are alloying elements in the ferritic weld metal [24]. The multiphase oxide inclusions fulfill the Griffith criterion of brittle fracture initiation. The particle may be brittle because of the intrinsic crystal structure or the preceding small defects within the inclusion. Therefore, the inclusion is likely to crack in the presence of plastic strain and further initiate a cleavage fracture. In the case of other ductile oxy-sulfides, debonding at the interfaces between uncracked inclusions and weld metal matrixes can induce further brittle fracture. Debonding can be regarded as a result of mild thermal aging, which is too minimal to affect mechanical properties but is strong enough to cause debonding rather than particle cracking at the brittle fracture initiation site. The effect of thermal aging below 300°C on debonding that causes microcracking still requires further studies.

5. Conclusions

A thermally-aged high Ni low-alloyed weld metal from a decommissioned boiling water reactor RPV head was investigated. Thermal aging did not change the impact toughness of the weld metal. The microstructure characterization, inclusion analysis, and fractographic examination revealed the effects of the microstructure and secondary particles on the brittle fracture initiation. The main findings are as follows.

(1) The as-welded microstructure consisted mainly of acicular ferrite. The reheated microstructure consisted mainly of polygonal ferrite. Small fractions of grain boundary ferrite were observed. The amount of grain boundary ferrite was associated with the observed IG- and ID-like fracture surfaces.

(2) The inclusion density in the as-welded region was approximately 1.5 times higher than that in the reheated region. The inclusions were mainly Fe–Mn–Al-containing (S)O complex compounds. All initiation sites in the investigated specimens with brittle fracture were located in the as-welded microstructure.

(3) Brittle fracture primarily initiated from inclusions with large sizes (0.5–2.5 μm) in all the CVN specimens tested at

the lower part of the transition curve. The cleavage fracture was initiated either within the brittle multiphase oxide inclusions or from the debonded interfaces between the uncracked inclusion and the weld metal matrix.

(4) The trend between particle size and location with impact energy was obtained. A low-impact energy was associated with the primary initiation site being closer to the V-notch and a large initiator particle size.

(5) The primary fracture sites can be determined in all the specimens tested in the lower part of the transition curve at and below the 41-J reference impact toughness energy but not above this point because of the changes in the fracture mechanism and the resulting changes in fracture appearance.

Acknowledgments

The authors gratefully acknowledge the BREDA program (Barsebäck Research and Development Arena) for providing the research material and the SAFIR2022 BRUTE project (Barsebäck RPV material used for true evaluation of embrittlement) for funding the study. The contributions and discussions with M. Boåsen from KTH, S. Lindqvist from VTT, and I. Virkkunen from Aalto University are acknowledged as well.

Open Access funding provided by VTT Technical Research Centre of Finland

References

[1] P. Haušild, C. Berdin, and P. Bompard, Prediction of cleavage fracture for a low-alloy steel in the ductile-to-brittle transition temperature range, *Mater. Sci. Eng. A*, 391(2005), No. 1-2, p. 188.

[2] A.H. Cottrell, Theory of brittle facture in steel and similar metals, *Trans. Metall. Soc. AIME*, 212(1958), p. 192.

[3] P. Joly, L. Sun, P. Efsing, J.P. Massoud, F. Somville, R. Gerard, Y.H. An, and J. Bailey, Characterization of in-service thermal ageing effects in base materials and welds of the pressure vessel of a decommissioned PWR pressurizer, after 27 years of operation, [in] *19th International Conference on Environmental Degradation of Materials in Nuclear Power Systems-Water Reactors 2019*, Boston, 2019, p. 392.

[4] K. Lindgren, M. Boåsen, K. Stiller, P. Efsing, and M. Thuvander, Evolution of precipitation in reactor pressure vessel steel welds under neutron irradiation, *J. Nucl. Mater.*, 488(2017), p. 222.

[5] Y.A. Nikolaev, A.V. Nikolaeva, A.M. Kryukov, V.I. Levit, and Y.N. Korolyov, Radiation embrittlement and thermal annealing behavior of Cr–Ni–Mo reactor pressure vessel materials, *J. Nucl. Mater.*, 226(1995), No. 1-2, p. 144.

[6] G.R. Odette and R.K. Nanstad, Predictive reactor pressure vessel steel irradiation embrittlement models: Issues and opportunities, *JOM*, 61(2009), No. 7, p. 17.

[7] R.S. Xing, D.J. Yu, G.F. Xie, Z.H. Yang, X.X. Wang, and X. Chen, Effect of thermal ageing on mechanical properties of a bainitic forging steels for reactor pressure vessel, *Mater. Sci. Eng. A*, 720(2018), p. 169.

[8] K. Wallin, M. Yamamoto, and U. Ehrnstén, Location of initiation sites in fracture toughness testing specimens: The effect of size and side grooves, [in] *Proceedings of the ASME 2016 Pressure Vessels and Piping Conference*, *Volume 1B: Codes and Standards*, Vancouver, 2016, art. No. V01BT01A011.

[9] A.A. Griffith, The phenomena of rupture and flow in solids, *Philos. Trans. R. Soc. London*, 221(1921), p. 163.

[10] A. Pineau, A.A. Benzerga, and T. Pardoen, Failure of metals I: Brittle and ductile fracture, *Acta Mater.*, 107(2016), p. 424.

[11] W. Weibull, A statistical theory of the strength of materials, [in] *Generalstabens Litografiska Anstalts Förlag*, Stockholm, 1939.

[12] W. Weibull, A statistical distribution function of wide applicability, *J. Appl. Mech.*, 18(1951), p. 293.

[13] F.M. Beremin, A. Pineau, F. Mudry, J.C. Devaux, Y. D'Escatha, and P. Ledermann, A local criterion for cleavage fracture of a nuclear pressure vessel steel, *Metall. Trans. A*, 14(1983), p. 2277.

[14] C.L. Briant and S.K. Banerji, Intergranular failure in steel: The role of grain-boundary composition, *Int. Met. Rev.*, 23(1978), No. 1, p. 164.

[15] R.W. Hertzberg, R.P. Vinci, and J.L. Hertzberg, *Deformation and Fracture Mechanics of Engineering Materials, 5th ed.*, John Wiley & Sons, Chichester, 2013. p. 299.

[16] J.D. Landes and D.H. Shaffer, Statistical characterization of fracture in the transition region, [in] P. Paris ed., *Fracture Mechanics*, ASTM International, West Conshohocken, 1980. p. 368.

[17] K. Wallin, *Fracture Toughness of Engineering Materials: Estimation and Application*, FESI Publishing, 2011.

[18] P. Bowen, S.G. Druce, and J.F. Knott, Effects of microstructure on cleavage fracture in pressure vessel steel, *Acta Metall.*, 34(1986), No. 6, p. 1121.

[19] H. Hein, J. Kobiela, M. Brumovsky, C. Huotilainen, J. Lydman, B. Marini, B. Radiguet, O. Startsev, M. Serrano Garcia, R. Hernandez Pascual, F. Roeder, and H.W. Viehrig, Addressing of specific uncertainties in determination of RPV fracture toughness in the SOTERIA project, [in] *Fontevraud 9-Contribution of Materials Investigations and Operating Experience to Light Water NPPs' Safety, Performance and Reliability*, Avignon, 2018.

[20] M. Boåsen, *Modeling of Structural Integrity of Aged Low Alloy Steels Using Non-Local Mechanics*, [Dissertation], KTH Royal Institute of Technology, Stockholm, Sweden, 2020.

[21] C.A. Hippsley and S.G. Druce, The influence of phosphorus segregation to particle/matrix interfaces on ductile fracture in a high strength steel, *Acta Metall.*, 31(1983), No. 11, p. 1861.

[22] H. Bhadeshia and R. Honeycombe, *Steels: Microstructure and Properties*, 4th ed. Elsevier Ltd., Cambridge, 2017.
[23] G.M. Evans, Effect of manganese on the microstructure and properties of all-weld-metal deposits, *Welding Res. Suppl.*, 59(1980), No. 3, p. 67.
[24] J.H. Shim, Y.J. Oh, J.Y. Suh, Y.W. Cho, J.D. Shim, J.S. Byun, and D.N. Lee, Ferrite nucleation potency of non-metallic inclusions in medium carbon steels, *Acta Mater.*, 49(2001), No. 12, p. 2115.
[25] B.A. Gurovich, E.A. Kulehsova, Y.I. Shtrombakh, O.O. Zabusov, and E.A. Krasikov, Intergranular and intragranular phosphorus segregation in russian pressure vessel steels due to neutron irradiation, *J. Nucl. Mater.*, 279(2000), No. 2-3, p. 259.
[26] D.J. Sprouster, J. Sinsheimer, E. Dooryhee, S.K. Ghose, P. Wells, T. Stan, N. Almirall, G.R. Odette, and L.E. Ecker, Structural characterization of nanoscale intermetallic precipitates in highly neutron irradiated reactor pressure vessel steels, *Scripta Mater.*, 113(2016), p. 18.
[27] K. Lindgren, M. Boåsen, K. Stiller, P. Efsing, and M. Thuvander, Cluster formation in in-service thermally aged pressurizer welds, *J. Nucl. Mater.*, 504(2018), p. 23.
[28] J.S. Byun, J.H. Shim, Y.W. Cho, and D.N. Lee, Non-metallic inclusion and intragranular nucleation of ferrite in Ti-killed C–Mn steel, *Acta Mater.*, 51(2003), No. 6, p. 1593.
[29] D.S. Sarma, A.V. Karasev, and P.G. Jönsson, On the role of non-metallic incluisons in the nucleation of acicular ferrite in steels, *ISIJ Int.*, 49(2009), No. 7, p. 1063.
[30] U. Zerbst, R.A. Ainsworth, H.T. Beier, H.T. Pisarski, Z.L. Zhang, K. Nikbin, T. Nitschke-Pagel, S. Münstermann, P. Kucharczyk, and D. Klingbeil, Review on fracture and crack propagation in weldments—A fracture mechanics perspective, *Eng. Fract. Mech.*, 132(2014), p. 200.
[31] M. Boåsen, K. Lindgren, J. Rouden, M. Öberg, J. Faleskog, M. Thuvander, and P. Efsing, Thermal ageing of low alloy steel weldments from a Swedish nuclear power plant—A study of mechanical properties, [in] *Fontevraud 9-Contribution of Materials Investigations and Operating Experience to Light Water NPPs' Safety, Performance and Reliability*, Avignon, 2018.
[32] M.K. Miller, K.A. Powers, R.K. Nanstad, and P. Efsing, Atom probe tomography characterizations of high nickel, low copper surveillance RPV welds irradiated to high fluences, *J. Nucl. Mater.*, 437(2013), No. 1-3, p. 107.
[33] Finnish Standards Association, ISO 148-1: 2016: *Metallic Materials—Charpy Pendulum Impact Test —Part 1: Test Method, Standard*, Finnish Standards Association, West Conshohocken, 2016.
[34] ASTM International, ASTM E185 -16: *Standard Practice for Design of Surveillance Programs for Light-Water Moderated Nuclear Power Reactor Vessels*, Standard, ASTM International, West Conshohocken, 2018.
[35] N. Hytönen, *Effect of Microstructure on Brittle Fracture Initiation in a Reactor Pressure Vessel Weld Metal* [Dissertation], University of Tampere, Tampere, 2019.
[36] S.J. Jones and H.K.D.H. Bhadeshia, Competitive formation of inter- and intragranularly nucleated ferrite, *Metall. Mater. Trans. A*, 28(1997), No. 10, p. 2005.
[37] T.L. Anderson, *Fracture Mechanics Fundamentals and Applications*, 2nd ed., CRC Press, Boca Raton, 1995.
[38] M. Kroon and J. Faleskog, Micromechanics of cleavage fracture initiation in ferritic steels by carbide cracking, *J. Mech. Phys. Solids*, 53(2005), No. 1, p. 171.
[39] L.F. Zhang, B. Radiguet, P. Todeschini, C. Domain, Y. Shen, and P. Pareige, Investigation of solute segregation behaviour using a correlative EBSD/TKD/APT methodology in a 16MND5 weld, *J. Nucl. Mater.*, 523(2019), p. 434.

J. Mech. Phys. Solids 147 (2021) 104224

Contents lists available at ScienceDirect

Journal of the Mechanics and Physics of Solids

journal homepage: www.elsevier.com/locate/jmps

A weakest link model for multiple mechanism brittle fracture — Model development and application

Magnus Boåsen *, Carl F.O. Dahlberg, Pål Efsing, Jonas Faleskog

Solid Mechanics, Department of Engineering Mechanics, KTH Royal Institute of Technology, Teknikringen 8D, SE-100 44 Stockholm, Sweden

ARTICLE INFO

Keywords:
Brittle fracture
Cleavage fracture
Intergranular
Transgranular
Crystal plasticity
Weakest link

ABSTRACT

A multiple mechanism weakest link model for intergranular and transgranular brittle fracture is developed on the basis of experimental observations of a thermally aged low alloy steel. The model development is carried out in tandem with micro mechanical analysis of grain boundary cracking using crystal plasticity modeling of polycrystalline aggregates with the purpose to inform the weakest link model. The fracture modeling presented in this paper is carried out by using a non-local porous plastic Gurson model where the void volume fraction evolution is regularized over two separate length scales. The ductile crack growth preceding the final brittle fracture is well predicted using this type of modeling. When applied to the brittle fracture tests, the weakest link model predicts the fracture toughness distribution remarkably well, both in terms of the constraint and the size effect. Included in the study is also the analysis of a reference material.

1. Introduction

The structural integrity of a component is fundamentally dependent on the mechanical properties of the material of which it is made. In the case of components of ferritic steels, cleavage fracture is an adverse failure mode that generally occurs at low temperatures. At higher temperatures, such materials progressively become more ductile until the cleavage failure mode is suppressed in its entirety. This transition is typically called the ductile-to-brittle transition and needs to be accounted for in the design and operation of components made from ferritic steels. For components with a long design life, the risk of embrittlement of structural materials by ageing due to environmental factors is increased. Such factors could be operating temperature, irradiation or a reactive chemical environment. Embrittlement of ferritic steels, which typically exhibit cleavage fracture at low temperatures, will cause an increase in the temperature at which cleavage fracture can occur. This phenomena is a characteristic for ageing of low alloy steels in nuclear power plants whereby ageing is primarily induced by neutron irradiation (Was, 2007) and high operating temperatures (Nanstad et al., 2018). Embrittlement by ageing in this sense is commonly divided into two groups; hardening and non-hardening embrittlement. Hardening embrittlement occurs due to the formation of microstructural features such as solute clusters or fine scale precipitates that impede dislocation motion, thereby increasing the yield strength of the material, resulting in embrittlement. Non-hardening embrittlement works by decreasing the cohesive strength of prior austenite grain boundaries by impurity segregation, thus altering the fracture path from the cleavage planes to the grain boundaries. The most common impurity elements known to cause this phenomenon belongs to groups IV-VI in the periodic system, e.g. P, S, Sn and Si, commonly found as trace elements in the steels considered (Briant and Banerji, 1978; Knott, 1977). Briant and Banerji (1978) also observed that with larger grain size came a larger fraction of intergranular failure, which they discussed in terms of dilution of segregants for the case

* Corresponding author.
E-mail address: boasen@kth.se (M. Boåsen).

https://doi.org/10.1016/j.jmps.2020.104224
Received 2 July 2020; Received in revised form 25 September 2020; Accepted 7 November 2020
Available online 13 November 2020
0022-5096/

of smaller grains, i.e. less impurities per unit grain boundary area. Both the hardening and non-hardening mechanisms can appear exclusive of the other or simultaneously. A recent study (Boåsen et al., 2020) of a weld metal from a decommissioned component from a Swedish nuclear power plant subjected to thermal ageing concluded that the material had been subject to both hardening as well as non-hardening embrittlement. Fracture toughness testing of the material revealed that multiple mechanisms for cleavage initiation existed, giving rise to a complex bimodal toughness distribution.

For cleavage fracture to be possible, several pre-requisites needs to be fulfilled. The first being the nucleation of a micro crack, this event typically occurs by the cracking of a second phase particle due to plastic straining of the matrix surrounding the particle (McMahon and Cohen, 1965). For a nucleated micro crack to transition into a fully developed cleavage crack experiencing unstable propagation it must grow in size and overcome microstructural barriers such as grain boundaries. This progression from nucleus to self-sustained growth will only be completed when a high enough stress level is reached over a sufficiently large region around the nucleation site. As cleavage fracture exhibits a large degree of inherent scatter, probabilistic modeling is needed to describe its behavior. Weakest link modeling has been shown to be well suited to describe the fracture toughness associated with cleavage fracture, examples of such models include the ones by Beremin et al. (1983), Wallin (1984), ASTM (2019a), Bordet et al. (2005a,b), and Kroon and Faleskog (2002), Faleskog et al. (2004), Kroon et al. (2008), Boåsen et al. (2019). These models have varying degree of complexity and different strengths, e.g. the *master curve* model by Wallin is based on the intensity, K_{I}, of the crack tip stress field and has been shown in numerous cases to well describe the strong effect of temperature on the cleavage fracture toughness. The model by Kroon and Faleskog has been shown to capture the effects of crack tip constraint in a promising way. However, all of the mentioned models pertain to single mechanism cleavage failure, i.e. brittle cleavage fracture initiated by one mechanism.

Models incorporating multiple mechanism brittle fracture include the one by Yahya et al. (1998) where the studied material displayed intergranular failure initiated at MnS-inclusions and transgranular failure initiated from a second population of microstructural features. The probabilistic model employed in their study is an extension of the Beremin model (Beremin et al., 1983). Another multiple mechanism model is the one by Wallin et al. (2004) which is an extension of the master curve model, making it capable of describing bimodal toughness distributions.

The material considered in this study is a multi-layer weld of a low alloy steel, where an understanding of the grain structures is of importance. As a multi-layer weld is formed, zones of different grain structures will emerge due to the solidification and subsequent reheating of the weld beads. As a weld bead solidifies during welding, a dendritic grain structure emerges transverse to the welding direction. When the multi-layer weld is built up, subsequent weld beads will be laid on top of the already existing beads, thus effectively heat treating the upper part of the weld bead below. This gives rise to a region with smaller equiaxed grains in the bead below due to recrystallization from the locally increased temperature. As this process continues, the weld will achieve a microstructure that has regions of dendritic grains, regions with finer grains that have been reheated once (equiaxed) and regions that have been reheated several times (equiaxed).

This paper is concerned with a probabilistic model for multiple mechanism brittle fracture where initiation is possible from both particle cracking as well as grain boundary failure. The model will be shown capable of handling crack tip constraint as well as incorporating multiple mechanisms for brittle fracture initiation. The model will be applied and compared to fracture tests of thermally aged welds from a decommissioned pressurizer from a Swedish nuclear power plant (Boåsen et al., 2020) and its main features will be explored. The outline of the paper is as follows, Section 2 gives a brief account of the fracture tests, as well as the modeling of the same, Section 3 presents the foundation of the probabilistic model and the model assumptions, Section 4 presents a micro mechanical study of polycrystalline aggregates in order to motivate the failure characteristics of grain boundaries, Section 5 presents an application of the model to experiments and explores the model behavior, and finally the paper is concluded by a discussion of the model and the results in Section 6.

2. Material, experiment and fracture modeling

2.1. Material and experiment

The experimental series considered in this study can be found detailed in Boåsen et al. (2020), however a brief review will also be given here.

The materials considered in this paper are two low alloy steel welds from the Ringhals nuclear power plant in Sweden, one thermally aged material subjected to 345 °C for ∼215 000 h, and a reference material that has been subjected to 310–315 °C for ∼176 000 h. Even though the difference in operating temperature and time may appear minute, the effects of ageing are distinct, the embrittlement due to operation of the reference material is considered small or close to negligible in comparison to the thermally aged material. From here onward the thermally aged material will be denoted *R4PRZ* and the reference material *R3RPVH*.

The main emphasis of the experiments were the constraint effect on the brittle fracture toughness and how the constraint sensitivity would be impacted by embrittlement due to thermal ageing. To elucidate this, fracture test series with different crack tip constraint were conducted at temperatures where the high constraint fracture toughness of the two materials would coincide. The fracture test series was composed of T–S oriented, SEN(B)-specimens with dimensions W = 30 mm, B = 15 mm, and $a/W = \{0.5 \text{ and } 0.1\}$ i.e. both deep and shallow cracks. Deep corresponding to a state of high crack tip constraint and shallow for low crack tip constraint. Also included was a series of smaller specimens to be used as a size effect reference with, W = 14 mm, B = 7 mm, and $a/W = 0.5$. The temperatures that were chosen to yield similar brittle fracture toughness were −50 °C and −90 °C for R4PRZ and R3RPVH respectively.

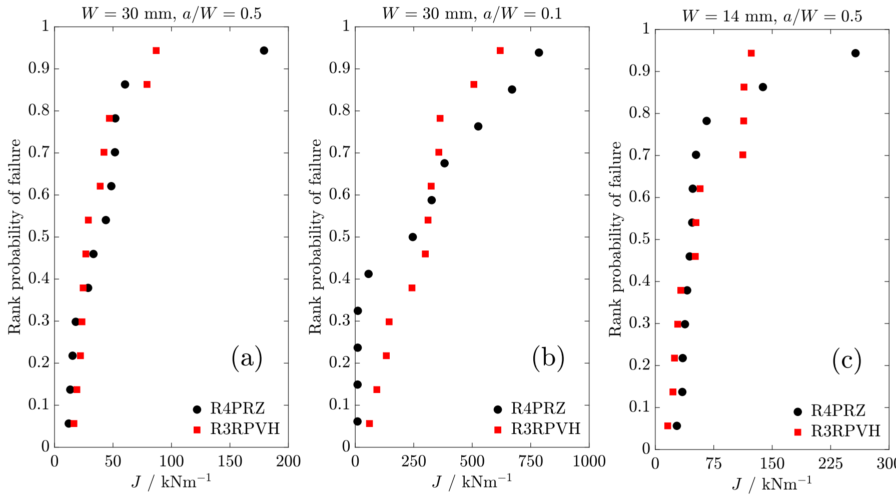

Fig. 1. Experimental fracture test results of the thermally aged R4PRZ and the reference R3RPVH. Results pertaining to high constraint specimens (a), low constraint specimens (b), and small specimens (c). (For interpretation of the references to colour in this figure legend, the reader is referred to the web version of this article.)

The reference temperature T_0 was determined from the fracture test results according to ASTM E1921 (ASTM, 2019a) to be $T_0^{\mathrm{R4PRZ}} = -33$ °C and $T_0^{\mathrm{R3RPVH}} = -78$ °C, i.e. a $\Delta T_0 = 45$ °C. The fracture tests of R4PRZ revealed a bimodal toughness distribution as seen in Fig. 1, where the effect on the specimens with shallow cracks was strong, as can be seen in the rank probabilities for the experimental data in Fig. 1. The rank probability of failure was estimated using the median rank according to Benard's approximation as $P^i_{\mathrm{rank}} = (i - 0.3)/(N + 0.4)$, where N is the number of specimens and i is the specimen in the series from 1 to N corresponding to P^i_{rank}. Fractographical investigations revealed that initiation of fracture in the more brittle specimens (low toughness) of R4PRZ, e.g. the first five specimens in Fig. 1(b), was exclusively from grain boundaries. In the specimens with higher fracture toughness, the brittle/cleavage fracture was preceded by ductile growth and was initiated partly from second phase particles and partly from grain boundaries. This revealed that two mechanisms exist in the microstructure and both can initiate brittle fracture. The testing of R3RPVH uncovered a unimodal toughness distribution with cleavage fracture initiation from second phase particles. It should be mentioned that small portions of intergranular features was found in a few specimens of the R3RPVH as well.

The experimental series also included ductile fracture tests that were conducted on the upper shelf at a temperature of 75 °C using SEN(B)-specimens with side-grooves to promote uniform growth along the crack front. The specimen dimensions were W = 30 mm, B = 15 mm, B_{N} = 12 mm, and $a/W = 0.5$. The ductile initiation fracture toughness was determined to J_{IC} = 338 kN/m for both materials at 75 °C.

2.2. Fracture modeling

Models of the experiments for both the development of the multiple mechanism weakest link model and the ductile failure tests were set up as finite element (FE) models. These were generated with meshes containing 32 500–47 000 elements for models pertinent to both the ductile fracture and brittle fracture experiments. Eight noded hexahedral elements with reduced integration was used in all models, and due to symmetry, only a quarter of the three point bend specimen was modeled with 12 elements through the thickness. An overview of the FE-models can be seen in Fig. 2. The elastic–plastic material behavior was modeled using the Gurson model for porous plasticity (Gurson, 1977) with the plastic potential under isotropic strain hardening as

$$\Phi = \left(\frac{\sigma_{\mathrm{e}}}{\sigma_{\mathrm{f}}}\right)^2 + 2\, q_1 f \cosh\left(\frac{3}{2}\frac{q_2\,\sigma_{\mathrm{m}}}{\sigma_{\mathrm{f}}}\right) - \left(1 + \left(q_1\, f\right)^2\right) = 0. \tag{1}$$

Here σ_{e} is the von Mises equivalent stress, σ_{m} is the mean stress, σ_{f} is the material flow strength, f is the void volume fraction, and q_1 and q_2 are parameters introduced by Tvergaard (1981, 1982) to improve model predictions. The parameters q_1 and q_2 will here be taken as proposed by Faleskog et al. (1998). The evolution of the void volume fraction during plastic straining is divided in two terms, one defined by dilatational deformation $\dot{f}_{\mathrm{m}}$ and one defined by deviatoric deformation $\dot{f}_{\mathrm{s}}$, i.e. $\dot{f} = \dot{f}_{\mathrm{m}} + \dot{f}_{\mathrm{s}}$. Contributions from nucleation due to plastic straining is also included but is split into the aforementioned categories as will be shown below. The evolution of the void volume fraction due to dilatational deformation is given by

$$\dot{f}_{\mathrm{m}} = (1 - f)\,\dot{\varepsilon}^{\mathrm{p}}_{\mathrm{kk}} + \dot{f}^{\mathrm{nucleation}}_{\mathrm{m}}, \tag{2}$$

where $\dot{\varepsilon}^{\mathrm{p}}_{\mathrm{kk}}$ is the volumetric part of the plastic strain increment. The evolution of the void volume fraction due to deviatoric deformation was first introduced by Nahshon and Hutchinson (2008) as a shear modification to the original Gurson model and

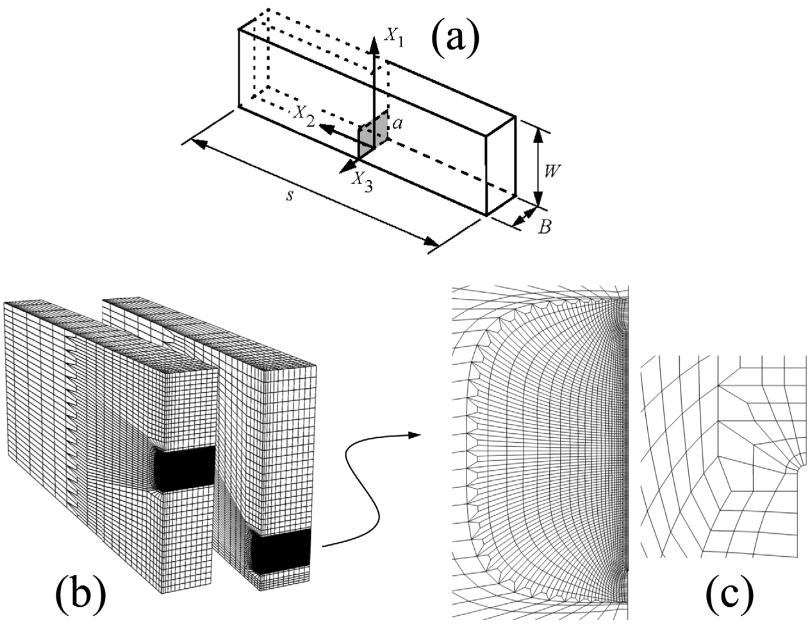

Fig. 2. (a) Schematic illustration of model symmetries and dimensions corresponding to experimental specimens, (b) illustration of finite element discretization, (c) close up of fine mesh region surrounding the vicinity of the crack tip.

is given by

$$\dot{f}_{\mathrm{s}} = k_\omega f \omega \frac{s_{ij}\dot{\varepsilon}^{\mathrm{p}}_{ij}}{\sigma_{\mathrm{e}}} \varphi(T) + \dot{f}^{\mathrm{nucleation}}_{\mathrm{s}}. \tag{3}$$

Here k_ω is a model parameter that sets the strength of the deviatoric damage evolution, s_{ij} is the stress deviator, $\dot{\varepsilon}^{\mathrm{p}}_{ij}$ is the incremental plastic strain tensor, ω is a measure of the stress state that is unity for a pure shear stress state with a smooth transition to zero as the stress state transitions to pure tension or compression. It is given by

$$\omega = 1 - \left(\frac{27J_3}{2\sigma_{\mathrm{e}}^3}\right)^2, \tag{4}$$

where J_3 is the third invariant of the stress deviator. The function $\varphi(T)$ penalizes the deviatoric damage evolution for high stress triaxialities T and was introduced by Nielsen and Tvergaard (2010) as the shear modification of the void volume fraction tends to overestimate the contribution at moderate to high stress triaxialities T. The function $\varphi(T)$ is here taken as

$$\varphi(T) = \frac{1}{2} - \frac{1}{2}\tanh\left(\kappa\left(T - T_\omega\right)\right), \tag{5}$$

which is unity for low values of T and transitions smoothly to zero depending on κ and T_ω. In this case, κ was calculated so that 90% of the transition from unity to zero would occur over the interval specified by ΔT_{90}, the relation becomes $\kappa = 1.4722195/\Delta T_{90}$.

The contribution to the void growth as a result of nucleation due to plastic straining is expressed as

$$\dot{f}^{\mathrm{nucleation}} = D\dot{\bar{\varepsilon}}^{\mathrm{p}}, \tag{6}$$

where $\dot{\bar{\varepsilon}}^{\mathrm{p}}$ is the matrix equivalent plastic strain rate which is related to the aggregate equivalent plastic strain rate as $\dot{\bar{\varepsilon}}^{\mathrm{p}} = \sigma_{ij}\dot{\varepsilon}^{\mathrm{p}}_{\mathrm{ij}} / \left[(1-f)\sigma_{\mathrm{f}}\right]$. This enables the separation into dilatational and deviatoric contributions as

$$\dot{f}^{\mathrm{nucleation}}_{\mathrm{m}} = D\frac{\sigma_{kk}\dot{\varepsilon}^{\mathrm{p}}_{\mathrm{kk}}}{3(1-f)\sigma_{\mathrm{f}}}, \tag{7}$$

$$\dot{f}^{\mathrm{nucleation}}_{\mathrm{s}} = D\frac{s_{ij}\dot{\varepsilon}^{\mathrm{p}}_{\mathrm{ij}}}{(1-f)\sigma_{\mathrm{f}}}. \tag{8}$$

Here D is the parameter for strain-controlled void nucleation at the current accumulated level of matrix equivalent plastic strain $\bar{\varepsilon}^{\mathrm{p}}$, which in this case is taken as a log-normal distribution as

$$D = \frac{f_{\mathrm{N}}}{\bar{\varepsilon}^{\mathrm{p}} s_{\mathrm{N}}\sqrt{2\pi}} \exp\left(-\frac{1}{2}\left[\frac{\ln\left(\bar{\varepsilon}^{\mathrm{p}}/\varepsilon_{\mathrm{N}}\right)}{s_{\mathrm{N}}}\right]^2\right). \tag{9}$$

The parameter f_N is related to the volume fraction available for nucleation, ε_N and s_N are the distribution parameters and relates to the mean and the standard deviation as $\varepsilon_\mu = \varepsilon_N \exp\left(s_N^2\right)$ and $s_D = \varepsilon_N \exp\left(s_N^2\right)\sqrt{\exp\left(s_N^2\right)-1}$, respectively. In the first formulation of strain controlled nucleation of voids by Chu and Needleman (1980) a normal distribution was employed. The present choice was made for two reasons (i) the normal distribution is defined for infinitely large negative plastic strains, and (ii) the underlying distributions of potential void forming features, such as second phase particles e.g. carbides, tend to be well described by a log-normal distribution.

As the void volume fraction f increases, the load carrying capacity will be reduced due to a material softening. This will give rise to mesh dependent solutions (cf. Zienkiewicz and Taylor, 1991). One solution to this issue in earlier studies of fracture modeling employing the Gurson model has been by use of careful mesh design where the element size becomes a material parameter, cf. Xia and Fong Shih (1995), and Gao et al. (1998). Another solution to this issue is suggested by Tvergaard and Needleman (1995) where the void volume fraction is regularized by integration over a certain length scale which yields mesh independent results. A third solution is exemplified by Nguyen et al. (2020) where a non-local micromorphic continuum theory is used in conjunction with the Gurson model, in their model the plastic strains are non-local variables which are then used to form the increment in the void volume fraction.

In the formulation presented here, the integration of void volume fraction is used where the dilatational and deviatoric components of the increment in the void volume fraction are regularized over separate length scales, R_m and R_s respectively. This is carried out as

$$\dot{\bar{f}}_m = \frac{1}{W_m\left(X_k\right)} \int_V \dot{f}_m\left(\hat{X}_k\right) w_m\left(X_k - \hat{X}_k\right) \mathrm{d}V, \tag{10a}$$

$$\dot{\bar{f}}_s = \frac{1}{W_s\left(X_k\right)} \int_V \dot{f}_s\left(\hat{X}_k\right) w_s\left(X_k - \hat{X}_k\right) \mathrm{d}V, \tag{10b}$$

where

$$W_i\left(X_k\right) = \int_V w_i\left(X_k - \hat{X}_k\right) \mathrm{d}V. \tag{11}$$

Here subscript i corresponds to the dilatational and deviatoric damage processes. The function $w_i\left(X_k\right)$ assumes the value of unity if $\left(X_k - \hat{X}_k\right) \leqslant R_i$ and zero if $\left(X_k - \hat{X}_k\right) > R_i$, where R_i is the dilatational length scale R_m in (10a) and the deviatoric length scale R_s in (10b). In this study, the w_i-function is a constant function over the non-local length scales, however, it can be readily chosen as a weight function as done by Tvergaard and Needleman (1995) or as for the non-local stress integration by Kroon et al. (2008). Note that $\dot{\bar{f}}_i$ will be equal to the local $\dot{f}_i$ in the limit where $R_i \to 0$. The integration is carried out in the reference configuration. The increment in void volume fraction used in all computations is the sum of the non-local increments as $\dot{f} = \dot{\bar{f}}_m + \dot{\bar{f}}_s$.

The reason for choosing this modeling approach was due to the mesh refinement needed for resolving the crack tip fields appropriately for the weakest link modeling. For instance, incorporating the constitutive length scale in the mesh design will not be able to resolve the fields accurately enough as this would yield too large elements for weakest link calculations, making the integration method more suited for the problem. The non-local regularization was initially carried out using a single length scale for the increment in void volume fraction. However, this proved to be problematic since the crack growth would consistently initiate some distance ahead of the crack tip and, in some cases depending on the choice of parameters, leave a small ligament of load carrying elements close to the crack tip. By separating the regularization into dilatational and deviatoric contributions to the void volume fraction, these problems could be avoided altogether.

As voids grow to a critical size during plastic straining, the load carrying capacity of the material point is diminished due to the coalescence of voids. This final process of void growth and failure is not captured by the Gurson model, instead the yield condition is evaluated using the modified void volume fraction f^* as introduced by Tvergaard and Needleman (1984) to account for the rapid increase in the void volume fraction during coalescence as

$$f^* = \begin{cases} f & \text{for } f \leqslant f_C \\ f_C + \frac{1/q_1 - f_C}{f_E - f_C}\left(f - f_C\right) & \text{for } f > f_C \end{cases} \tag{12}$$

where f_C is the critical void volume fraction at the onset of coalescence and f_E is the void volume fraction at total loss of load carrying capacity.

The incremental constitutive model has been implemented in the commercial software Abaqus as a VUMAT. Further details about the model implementation and behavior will be not be elaborated on here. Regarding the boundary conditions of the FE-models, symmetry conditions were prescribed on the planes $X_2 = 0$ and $X_3 = 0$ by enforcing $u_2 = 0$ and $u_3 = 0$, respectively. The top roller support of the SEN(B)-specimen set up was modeled by enforcing $u_1 = 0$ at the three top node rows in the plane $X_2 = 0$. The load was introduced by applying a constant velocity $v_1 = \bar{v}_1$ at $\{X_1 = 0, X_2 = 2W\}$, $\bar{v}_1$ was specified at a level to achieve a solution judged to be close to quasi-static. All models were solved using large deformations. In Abaqus Explicit, the J-integral cannot be calculated by the built in routines. Instead, the J-integral was calculated from the force-load line displacement relation according to the methodology supplied in ASTM E1820 (ASTM, 2019b) along with the relation for the plastic η-factor for shallow cracks from Faleskog et al. (2004).

The material flow strength was inferred from tensile tests of the weld metals and was fitted to a Voce-like hardening law on the form

$$\sigma_f = \sigma_0\left[1 + \alpha_f\,\bar{\varepsilon}^p + \beta_f\,\left(1 - \exp\left(-\gamma_f\,\bar{\varepsilon}^p\right)\right)\right], \tag{13}$$

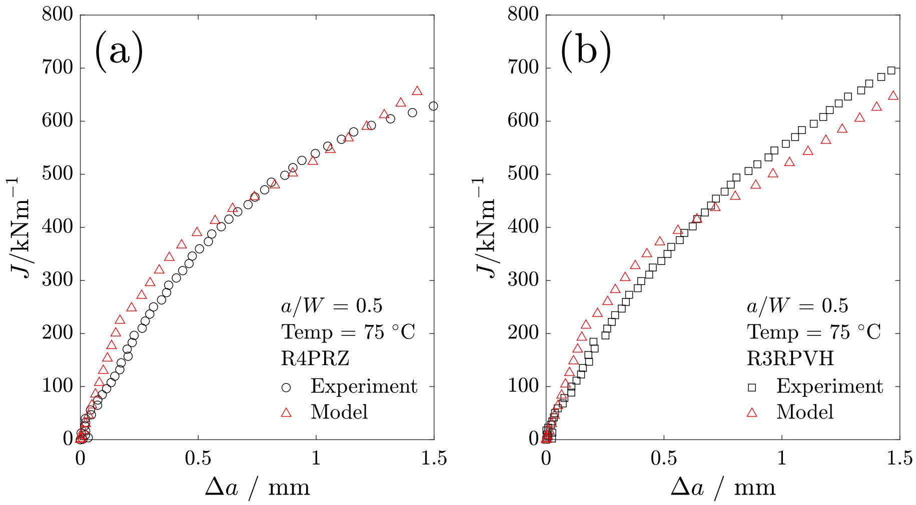

Fig. 3. Comparison of crack growth predictions and experimental fracture test results at test temperature 75 °C. (a) Thermally aged R4PRZ, (b) reference R3RPVH. Note, these data sets were used for parameter calibration. (For interpretation of the references to colour in this figure legend, the reader is referred to the web version of this article.)

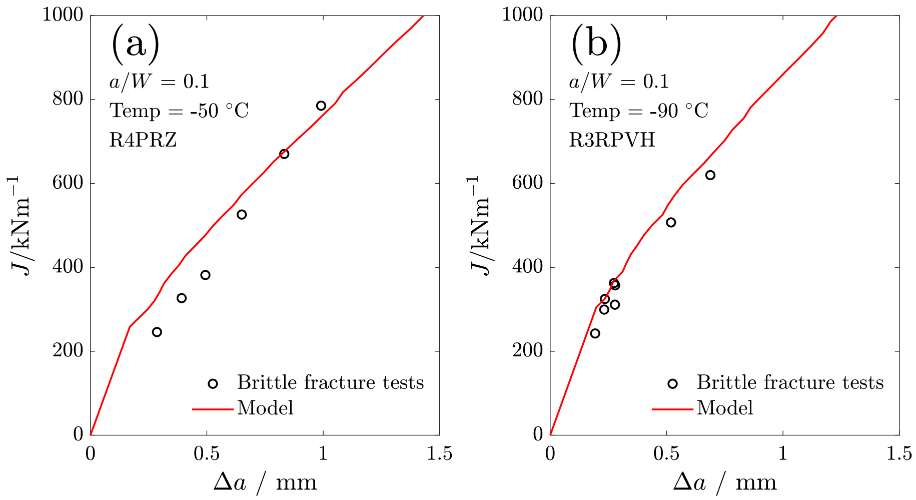

Fig. 4. Comparison of crack growth predictions and experimental fracture test results at test temperatures −50 °C and −90 °C. (a) Thermally aged R4PRZ, (b) reference R3RPVH. (For interpretation of the references to colour in this figure legend, the reader is referred to the web version of this article.)

where σ_0, α_f, β_f and γ_f are parameters that can be found in Table 1.

The parameters of the porous plastic model were calibrated from the ductile fracture tests at 75 °C, and then used to make predictions which were compared to the fracture test results at −50 and −90 °C. The parameters can be found in Table 2. The same model parameters pertinent to the porous plastic models were used for both materials. The comparison between experimental results and model predictions can be seen in Figs. 3 and 4 for the ductile fracture tests and the brittle specimens subjected to ductile growth prior to final brittle failure, respectively. A comparison between the force–displacement relation of the brittle fracture specimens can be seen in Fig. 5. Models of different levels of discretization were used in the modeling of the pure ductile fracture tests and the brittle fracture tests. The pertinent issue here is to note the resolution in the integrals of (10a) and (10b). For the length scales in Table 2, the models used for the pure ductile simulations has a level of discretization that gives ~20 elements/element for the dilatational length scale and ~3 elements/element for the deviatoric length scale, along the axis of crack propagation in the fine mesh zone respectively. The corresponding numbers for the finer models used in the modeling of the brittle fracture tests are ~28 elements/element for the dilatational length scale and ~5 elements/element for the deviatoric length scale, along the axis of crack propagation in the fine mesh zone.

In order to supply relevant boundary conditions for the micromechanical model in Section 4, the stress state ahead of the crack tip in the relevant models will be analyzed. Any stress state can be described by its three principal stresses, or correspondingly by a combination of the von Mises effective stress σ_e, the triaxiality parameter, $T = (\sigma_I + \sigma_{II} + \sigma_{III})/(3\sigma_e)$, and the Lode parameter,

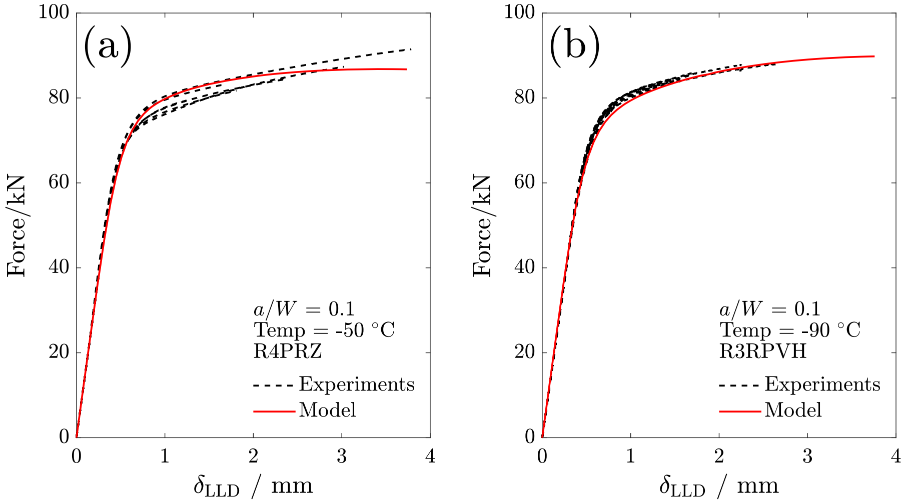

Fig. 5. Comparison of force–displacement predictions and experimental fracture test results at test temperatures −50 °C and −90 °C. (a) Thermally aged R4PRZ, (b) reference R3RPVH. (For interpretation of the references to colour in this figure legend, the reader is referred to the web version of this article.)

Table 1
Model parameters used in the Voce-like hardening law.

Material	$T/°\mathrm{C}$	σ_0/MPa	α_f	β_f	γ_f
R4PRZ	75	662.0	0.3143	0.1541	20.97
R3RPVH	75	617.8	0.3393	0.1772	24.89
R4PRZ	−50	717.5	0.4098	0.2900	16.09
R3RPVH	−90	694.4	0.4772	0.3600	21.6

Table 2
Model parameters used in the porous plastic model.

Parameter	Value	Parameter	Value	Parameter	Value
q_1	1.57	q_2	0.974	f_0	0.003
k_ω	3.0	T_ω	0.9	ΔT_{90}	0.2
f_N	0.001	ε_N	0.03	S_N	0.5
f_C	0.15	f_E	0.2		
$R_m/\mu\mathrm{m}$	280	$R_s/\mu\mathrm{m}$	50		
E/GPa	200	ν	0.3		

$L = (2\sigma_{II} - \sigma_I - \sigma_{III})/(\sigma_I - \sigma_{III})$, where the characteristics of the stress state is determined by the combination of T and L. The maximum principal stress, the stress triaxiality and the Lode parameter were extracted ahead of the crack tip from the models of the specimens used in the testing in order to understand the characteristics of the stress state. The maximum principal stress was extracted rather than the von Mises effective stress since understanding of the highest stress and its location ahead of the crack tip is central for brittle fracture. To capture the effect of crack tip constraint on the stress state ahead of the crack tip, models with the crack size to width ratio $a/W = \{0.5, 0.1\}$ were used.

The stress state in terms of the maximum principal stress σ_I, the stress triaxiality T, and the Lode parameter L was extracted ahead of the crack tip along the centerline of the specimen and can be seen plotted against the normalized crack tip coordinate in Fig. 6(a-c). The specimen was loaded to levels that would not cause ductile crack growth, i.e. the solutions presented in Fig. 6 are representative for those of a stationary crack. Fig. 6(d-f) shows the same quantities averaged over the interval $0.5 \leqslant r\sigma_0/J \leqslant 2.0$, i.e. around the stress peak in Fig. 6(a-c), against the level of loading as defined through the J-integral. The difference in crack tip constraint is clearly shown in Fig. 6(a) and (b) where the shallow cracked specimen has a less intense stress state than the deeply cracked specimen. From subfigures (d-f) it is seen how the stress state undergoes a build-up period, reaching a close to constant level over the load levels depicted. From this analysis it was found that the stress state in the region around the stress peak in deeply and shallowly cracked SENB specimens could be characterized by $T = \{2.2, 1.9\}$ and $L = \{-0.25, -0.4\}$, respectively.

3. Probabilistic model incorporating multiple failure mechanisms

In this chapter a weakest link model capable of handling multiple mechanisms for brittle fracture will be developed.

As brittle failure is an inherently probabilistic process by nature which typically can be traced back to a single micro crack nucleus that developed into a self-sustaining brittle fracture, weakest link modeling is considered appropriate here. The basic weakest link

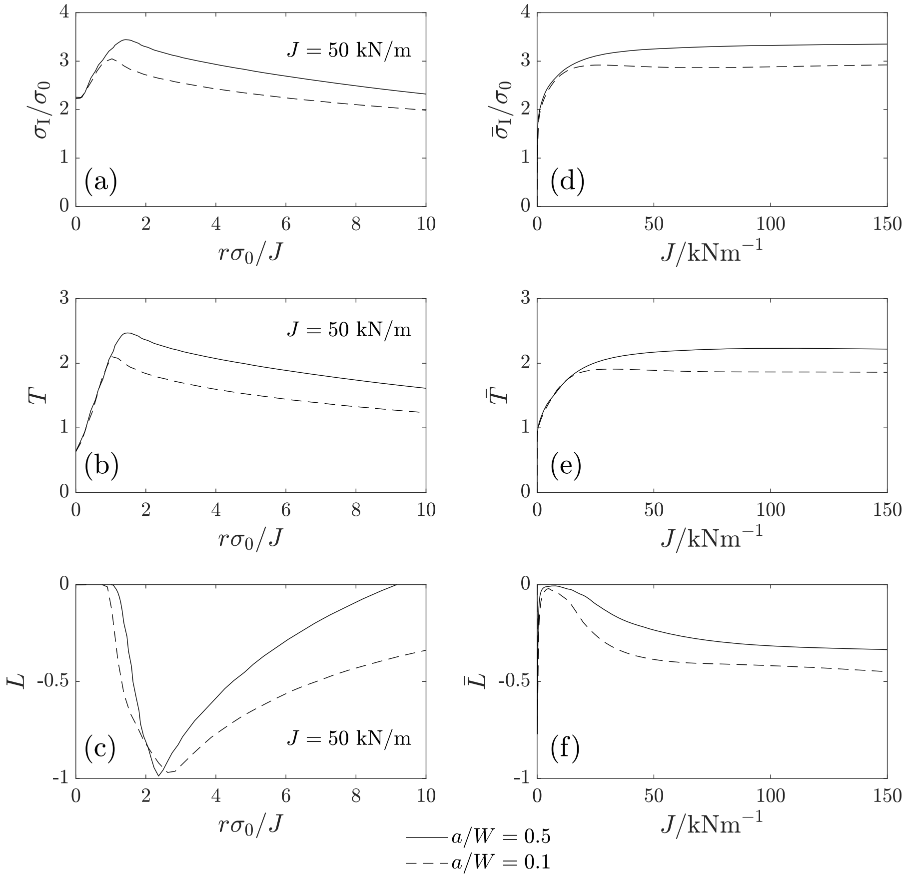

Fig. 6. Stress state characteristics along the centerline in the crack plane of the SEN(B)-specimen. (a) Maximum principal stress normalized with σ_0 from Eq. (13), (b) stress triaxiality T, and (c) Lode parameter L, (a-c) plotted at $J = 50$ kN/m. (d) Normalized averaged maximum principal stress, (e) averaged stress triaxiality $\bar{T}$, (f) averaged Lode parameter $\bar{L}$, (d-f) averaged over $0.5 \leqslant r\sigma_0/J \leqslant 2.0$ and plotted throughout the loading history.

assumption can be summarized as: the volume of a structure can be divided into infinitesimal elements, complete failure of the structure occurs if one of these elements fail. It will be assumed that one of two possible failure mechanisms may be activated within each element, specifically grain boundary or particle initiated failure. However, the following framework can readily be extended to a multitude of mechanisms. The nature of the problem allows for the expression of the probability of failure to be derived by assuming either statistical independence or mutual exclusivity among the failure mechanisms. If statistical independence is assumed, the probability of failure of an infinitesimal element can be written as $P(A \cup B) = P(A) + P(B) - P(A)P(B)$, which together with the assumption of small failure probabilities of each element becomes subject to $P(A)P(B) \approx 0$, resulting in the probability of failure of an element as $P(A \cup B) = P(A) + P(B)$. Mutual exclusivity implies that even though multiple mechanisms are probable to cause brittle fracture initiation, only one mechanism will initiate and cause the resulting failure, i.e. either the one or the other. Therefore, the probability of failure of an infinitesimal element can be written as $P(A \cup B) = P(A) + P(B)$, and thus $P(A \cap B) = 0$. This results in a weakest link expression as

$$P_{\mathrm{f}} = 1 - \exp\left(-\int_V \left(h^{\mathrm{A}} + h^{\mathrm{B}}\right) \frac{\mathrm{d}V}{V_0}\right), \tag{14}$$

where h^{A} and h^{B} are the hazard functions for the different micro mechanisms of failure. The connection between the physical behavior of the micro mechanism and the probabilistic model is described through the functions $h^i(\sigma, \varepsilon)$, which can be interpreted to be related to the number of potential brittle crack initiators available at the current load level. The superscript i is used to signify a specific micro mechanism. The model developed here takes inspiration from the work by Kroon and Faleskog (2002) and can be seen as a development of that model. In their work, the function h was divided into two separate parts as $h = h_1(\bar{\varepsilon}^{\mathrm{p}})\, h_2(\bar{\sigma})$, where h_1 is related to the formation of micro cracks and is representative of the number of micro cracks at that level of plastic strain, while h_2 is related to the propagation of a critical micro crack leading to macroscopic failure. In previous studies (Faleskog et al., 2004; Kroon et al., 2008; Boåsen et al., 2019) where this model has been applied, the failure probability was calculated from the maximum value of h during the load history leading up to the current load step. This choice makes the implementation straight forward and relatively simple, however it leaves the interpretation of h ambiguous in some cases. For example, if the micro crack nucleation rate would decrease with increasing plastic strain, the model would still predict an increasing probability of failure. Also, a micro crack needs to be nucleated in a region of high stress such that it keeps propagating until it can become self-sustaining. It is less likely that brittle fracture will occur from an arrested micro crack, which a model with $h_{\max}$ suggests. For this reason, an incremental formulation for h_1 is proposed as

$$h_1^i = \int_0^{\bar{\varepsilon}^{\mathrm{p}}} g_1^i\left(\bar{\varepsilon}^{\mathrm{p}}\right) \mathrm{d}\bar{\varepsilon}^{\mathrm{p}}, \tag{15}$$

where g_1 is related to the rate of nucleation of micro cracks. Combined with h_2, the expression for h becomes

$$h^i = \int_0^{\bar{\varepsilon}^{\mathrm{p}}} g_1^i\left(\bar{\varepsilon}^{\mathrm{p}}\right) h_2^i\left(\sigma\left(\bar{\varepsilon}^{\mathrm{p}}\right)\right) \mathrm{d}\bar{\varepsilon}^{\mathrm{p}}. \tag{16}$$

This expression allows for unambiguous interpretations of the nucleation rate and that a micro crack must indeed nucleate in a region of high stress in order to propagate as a cleavage crack. Experimental observations by McMahon and Cohen (1965), Lindley et al. (1970), and Gurland (1972) prompted Kroon and Faleskog to use a linear function for h_1 which in this framework translates to a constant g_1. The case of a linear h_1–function has been shown to work well in the case of particle initiated cleavage. A viable choice of g_1 for intergranular failure will be developed in Section 4. The function h_2 will for both mechanisms be taken to be on the same form as in the original model, i.e. through an assumption of an exponential micro crack size distribution as

$$h_2^i(\bar{\sigma}) = \begin{cases} \exp\left(-\left(\frac{\eta\sigma_{\mathrm{th}}^i}{\bar{\sigma}}\right)^2\right) - \exp\left(-\eta^2\right) \text{ for } \bar{\sigma} > \sigma_{\mathrm{th}}^i, \\ 0 \text{ for } \bar{\sigma} \leqslant \sigma_{\mathrm{th}}^i. \end{cases} \tag{17}$$

Here, σ_{th}^i is the threshold stress below which brittle fracture is not possible, $\bar{\sigma}$ is a non-local measure of stress. The parameter η is a distribution parameter which has been shown to have little significance in practical applications and η will be taken as unity throughout this study as per the suggestions in Kroon and Faleskog (2002). The non-local stress measure $\bar{\sigma}$ in (17) is calculated from the non-local stress tensor $\bar{\sigma}_{ij}$, which is calculated as the volume average over the volume V_{L} with radius L as

$$\bar{\sigma}_{ij} = \frac{1}{V_{\mathrm{L}}} \int_{V_{\mathrm{L}}} \sigma_{ij}(X_k - \hat{X}_k)\, \mathrm{d}\hat{V}, \tag{18}$$

where $\mathbf{X} = \left\{X_1, X_2, X_3\right\}$ are the coordinates of the center of V_{L} and $L \geqslant |X_k - \hat{X}_k|$. Note that $\bar{\sigma}_{ij}$ will be equal to the local σ_{ij} in the limit of $L \to 0$ or if the stress state in V_{L} is homogeneous. The non-local stress measure $\bar{\sigma}$ can then readily be calculated from the principal stresses of the non-local stress tensor as

$$\bar{\sigma} = \frac{(n+1)\bar{\sigma}_{\mathrm{I}} + \bar{\sigma}_{\mathrm{II}} + \bar{\sigma}_{\mathrm{III}}}{n+3}, \tag{19}$$

which is the effective normal stress measure, introduced in Boåsen et al. (2019), where the parameter n can be used to obtain a measure of normal stress that ranges between the mean stress when $n = 0$ and the maximum principal stress when $n \to \infty$. Note the ordering of the principal stresses $\bar{\sigma}_{\mathrm{I}} \geqslant \bar{\sigma}_{\mathrm{II}} \geqslant \bar{\sigma}_{\mathrm{III}}$. In this study, $n \to \infty$ was chosen, resulting in the maximum principal stress in order to reduce the parameter space.

At significant plastic straining related to the ductile failure process potential brittle fracture initiators may cause a void to form rather than initiating a brittle fracture nucleus. Either by particle debonding or by microcrack arrest of a grain boundary crack. A method to account for this process in the modeling of brittle fracture was laid out by Xia and Fong Shih (1996). By considering the conditional probability of brittle fracture occurring given that no void has nucleated, the brittle fracture probability given the probability of void nucleation can be written as

$$P_{\mathrm{brittle}}^i = P_{\mathrm{brittle}_{\mathrm{novoid}}}^i\left(1 - P_{\mathrm{void}}\right), \tag{20}$$

where P_{brittle}^i is the brittle fracture probability, $P_{\mathrm{brittle}_{\mathrm{novoid}}}^i$ is the brittle fracture probability where no account is taken of void nucleation, and P_{void} is the void nucleation probability. Taking this into account for the total failure probability alters the expression in Eq. (14) to

$$P_{\mathrm{f}} = 1 - \exp\left(-\int_V \left(h^A + h^B\right)\left(1 - P_{\mathrm{void}}\right) \frac{\mathrm{d}V}{V_0}\right). \tag{21}$$

Here it is assumed that both brittle mechanisms are affected in the same way where P_{void} is related to the nucleation of voids due to plastic straining as introduced in Section 2.2, which is expressed as

$$P_{\mathrm{void}} = \frac{1}{f_{\mathrm{N}}} \int_0^{\bar{\varepsilon}^{\mathrm{p}}} D\left(\bar{\varepsilon}^{\mathrm{p}}\right) \mathrm{d}\bar{\varepsilon}^{\mathrm{p}}. \tag{22}$$

The mechanisms of interest in this study are as observed experimentally in Section 2.1, namely brittle intergranular and transgranular cleavage fracture. In the weakest link modeling carried out in the remainder of the paper transgranular cleavage will be represented by mechanism A and brittle intergranular fracture will be mechanism B.

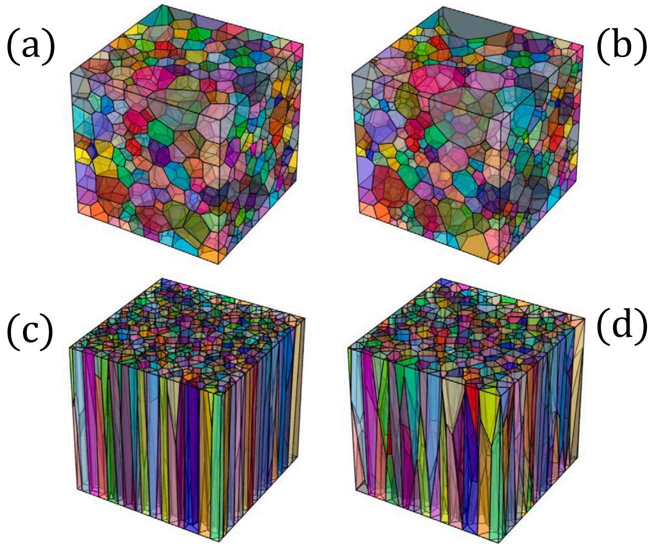

Fig. 7. Tesselations of grain structures. (a) and (b) corresponds to the equiaxed grain structures, where $c_v = \{0.2, 0.4\}$ respectively. (c) and (d) corresponds to the dendritic grain structures, where the aspect ratio of the grains corresponds to 0.05 and 0.1 respectively. (For interpretation of the references to colour in this figure legend, the reader is referred to the web version of this article.)

4. Modeling of grain boundary failure

Micro mechanical modeling of polycrystalline aggregates has been considered in order to study and motivate the micro crack nucleation rate from grain boundaries subjected to a stress state relevant to that of a material point ahead of a deforming crack tip. As a multi-layer weld is considered in this study, the grain structures have been divided into representative volume elements (RVEs) of equiaxed grains and dendritic grains. The grain structure models considered here were made using the open-source software Neper (Quey et al., 2011). The equiaxed grain structures were made using a constrained tesselation to yield a log-normal grain size distribution with a specific coefficient of variation $c_v = s/\mu$, and a log-normal grain sphericity distribution in order to achieve the equiaxed structure. The dendritic grain structures were constructed from tessellations with specific grain aspect ratios, asp = width/length. The grain structures considered in this study contain 1000 or 800 grains with random crystallographic orientation. For simplicity the equiaxed and dendritic structures were separated into individual models as depicted in Fig. 7.

4.1. Crystal plasticity

The analysis of the RVEs has been carried out using the crystal plasticity framework offered in the open-source software DAMASK (Roters et al., 2019). The crystal plastic framework in DAMASK is a modification of the phenomenological model introduced by Hutchinson (1976) to accommodate the slip systems of bcc crystals. The framework incorporates slip on 12 $\{110\}\langle 111\rangle$ and 12 $\{112\}\langle 111\rangle$ systems, respectively, which are parameterized by the slip resistances s^α $(\alpha = 1, 2, \dots, 24)$. The resistance is asymptotically increased from the initial critical resolved shear stress s_0^α towards the saturation stress s_∞^α due to shearing on the slip systems γ^β $(\beta = 1, 2, \dots, 24)$ as

$$\dot{s}^\alpha = \sum_{\beta=1}^{24} h_0 |\dot{\gamma}^\beta| \left| 1 - \frac{s^\beta}{s_\infty^\alpha} \right|^a \operatorname{sgn}\left(1 - \frac{s^\beta}{s_\infty^\alpha}\right) h^{\alpha\beta}, \tag{23}$$

where h_0 and a are model parameters and $h^{\alpha\beta}$ are slip interaction parameters. Given a set of current slip resistances and a resolved shear stress, the shear on each slip system evolves at a rate of

$$\dot{\gamma}^\alpha = \dot{\gamma}_0 \left| \frac{\tau^\alpha}{s^\alpha} \right|^n \operatorname{sgn}(\tau^\alpha), \tag{24}$$

where $\dot{\gamma}_0$ is the reference shear rate and n is the viscoplastic stress exponent. The resolved shear stress, τ^α, on a specific slip system is calculated as

$$\tau^\alpha = \mathbf{M}_\mathrm{p} \left(s_\mathrm{s}^\alpha \otimes n_\mathrm{s}^\alpha \right), \tag{25}$$

where $\mathbf{M}_\mathrm{p}$ is the Mandel stress in the intermediate plastic configuration, s_s^α and n_s^α are the unit vectors along the slip direction and the slip plane normal, respectively. The sum of all individual shear contributions on all slip systems defines the plastic velocity

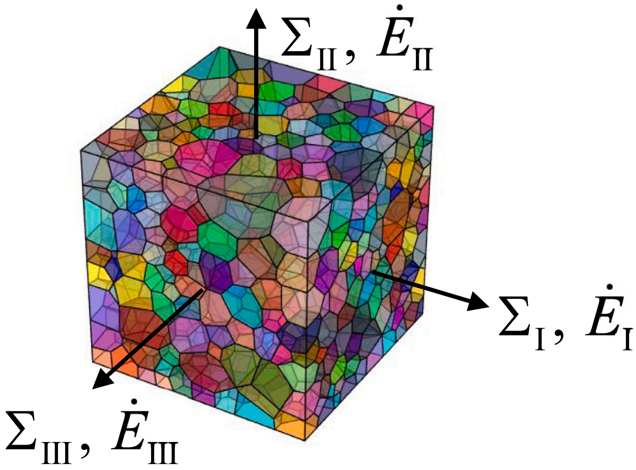

Fig. 8. Illustration of the principal axes of the RVE. (For interpretation of the references to colour in this figure legend, the reader is referred to the web version of this article.)

gradient, $\mathbf{L}_{\mathrm{p}}$, as

$$\mathbf{L}_{\mathrm{p}} = \sum_{i=1}^{24} \dot{\gamma}^{\alpha} \left(s_{\mathrm{s}}^{\alpha} \otimes n_{\mathrm{s}}^{\alpha} \right). \tag{26}$$

The elastic behavior is described by the generalized Hooke's law subjected to cubic symmetry, hence three independent parameters c_{11}, c_{12} and c_{44} describes the elastic properties of the microstructure. The elastic properties were chosen with anisotropy according to Hirth and Lothe (1982), but scaled to yield a homogenized Young's modulus of 200 GPa.

To study the crack initiation from grain boundaries using the models depicted in Fig. 7, appropriate boundary conditions relevant to the analysis are needed. However, applying displacement boundary conditions to achieve such a state in a finite deformation elastic–plastic analysis poses a problem as the volumetric behavior will change when the plastic deformation starts to dominate the solution. To overcome this issue, the RVEs are subjected to straining such that the macroscopic stress ratios over the RVE are kept constant through nonlinear kinematic constraints. Moreover, the sides of the model are constrained to remain straight and perpendicular during deformation. This is achieved through constraining the RVEs by a multi point constraint (MPC) in Abaqus. The procedure for this type of constraint was introduced by Faleskog et al. (1998) since then the methodology has been successfully applied in various formulations in several studies such as Kim et al. (2004), Barsoum and Faleskog (2007), Vadillo and Fernández-Sáez (2009), Dæhli et al. (2016), Liu et al. (2016) and Dæhli et al. (2017). This methodology makes it possible to supply the characteristics of the stress state in terms of the triaxiality parameter T and the Lode parameter L.

In order to estimate the crystal plastic model material parameters in Table 3, a model with $T = 1/3$ and $L = -1$ was utilized and compared to uniaxial tensile test data (before necking). The von Mises effective stress and strain used for the comparison was readily calculated from the macroscopic principal stresses and strain increments acting over the RVE as

$$\Sigma_{\mathrm{e}} = \frac{1}{\sqrt{2}} \sqrt{\left(\Sigma_{\mathrm{I}} - \Sigma_{\mathrm{II}}\right)^2 + \left(\Sigma_{\mathrm{II}} - \Sigma_{\mathrm{III}}\right)^2 + \left(\Sigma_{\mathrm{I}} - \Sigma_{\mathrm{III}}\right)^2}, \tag{27}$$

$$E_{\mathrm{e}}^{\mathrm{p}} = \int_0^t \frac{\sqrt{2}}{3} \sqrt{\left(\dot{E}_{\mathrm{I}}^{\mathrm{p}} - \dot{E}_{\mathrm{II}}^{\mathrm{p}}\right)^2 + \left(\dot{E}_{\mathrm{II}}^{\mathrm{p}} - \dot{E}_{\mathrm{III}}^{\mathrm{p}}\right)^2 + \left(\dot{E}_{\mathrm{I}}^{\mathrm{p}} - \dot{E}_{\mathrm{III}}^{\mathrm{p}}\right)^2}\,\mathrm{d}t, \tag{28}$$

where the principal axes are illustrated in Fig. 8. The constitutive crystal plastic model parameters were tuned until the model response was comparable to uniaxial tensile test data. The comparison between model response and tensile test data can be seen in Fig. 9. All parameters used in DAMASK can be found in Table 3.

4.2. Grain boundary stress state and micro crack nucleation

This section is dedicated to the study of grain boundary failure and its connection to the weakest link model, i.e. mechanism B in the model presented in Section 3. The simulations pertinent to the investigation of the grain boundary cracking were run with boundary conditions enforcing $T = \{2.35, 2.2, 2.05, 1.9, 1.75\}$ and $L = -0.25$. Early on in the investigation it was realized that the stress triaxiality T had a significant influence on the grain boundary stress state while the Lode parameter L had a negligible influence. Therefore, a range of stress triaxialities was chosen to enclose the values found in the analysis in Section 2.2 to be used as boundary conditions in the analysis of the polycrystalline aggregates.

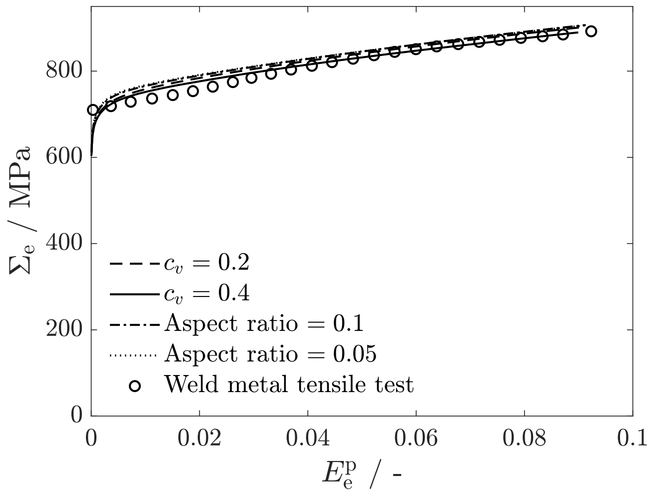

Fig. 9. Comparison between homogenized Σ_e-E_e^p over the RVE and the experimental flow stress–strain relation as inferred from a tensile test.

Table 3
Model parameters used in crystal plasticity model.

Parameter	Value	Parameter	Value
h_0/MPa	2700.0	n	50.0
$h^{\alpha\beta}$	1.4	a	15.0
s_0^α/MPa	290.0	c_{11}/GPa	184.0
s_∞^α/MPa	1850.0	c_{12}/GPa	107.0
$\dot{\gamma}_0$/s^{-1}	0.001	c_{44}/GPa	93.0

The initiation of a micro crack from a grain boundary capable of participating in a brittle failure event has been analyzed through assuming that the grain boundary strength can be associated to a surface energy, γ_s. The driving force to nucleate a micro crack at a grain boundary facet is assumed to be governed by the Griffith criterion (Griffith, 1921; Anderson, 2005), which relates the surface energy γ_s to a critical stress σ_c. Here, γ_s is viewed as an effective surface energy also including some plastic dissipation representative of grain boundary separation. For practical purposes, the shape of the grain boundary crack will be in the form of an internal elliptic crack, characterized by the grain boundary area A_{GB} and its aspect ratio $\kappa = a/c$, where a and c are the minor and major axis respectively. This yields the following expression for the grain boundary strength,

$$\sigma_c = \left(\frac{2\left(1/\sqrt{\kappa} + 1.464\kappa^{1.15}\right) E\gamma_s}{\pi\left(1-\nu^2\right)} \right)^{1/2} \left(\frac{\pi}{A_{GB}}\right)^{1/4}, \tag{29}$$

where the stress intensity solution was taken from Newman and Raju (1981). The surface energy used to compute the critical stress will be presented normalized according to $\bar{\gamma} = \gamma_s/(E\bar{d})$, where $\bar{d}$ is the mean radius of the grains calculated from the volume by assuming grains of spherical shape.

As detailed in Section 3, the relation between the incremental failure probability in a sub-volume of the structure and the physical process resulting in brittle fracture is described through the function h, which itself is divided into two parts, $h = h_1(\bar{\varepsilon}^p)\, h_2(\bar{\sigma})$. The first part is related to the number of micro cracks at a given level of plastic strain, which here will be formed on the basis of the nucleation rate, being the key issue in this analysis. Thus in the post-processing of the grain structure models, the normal stress component of the tractions, σ_n, between two grains is compared to the strength, σ_c, of that specific grain boundary to determine whether failure has occurred. If failure occurs, then that specific grain boundary is added to the cumulative number of failed grain boundaries not to be regarded in the subsequent load history. If failure does not occur, then it will be eligible for failure at a later stage in the load history. The main drawback of such an analysis it that even though a boundary has failed it will continue to carry load, as opposed to cohesive zone modeling where a load redistribution would occur at the moment of failure. However, it is presumed that this type of analysis can be justified for the understanding of h as long as the number fraction of grain boundaries considered to be critical is low. To achieve this, $\bar{\gamma} = 3.5 \cdot 10^{-5}$ was chosen and used throughout.

The fraction of critical grain boundaries, i.e. the accumulated number of grain boundaries that has exceeded the critical stress, normalized by the total number of grain boundaries in the analysis for all the considered models can be seen in Fig. 10. It is clear that

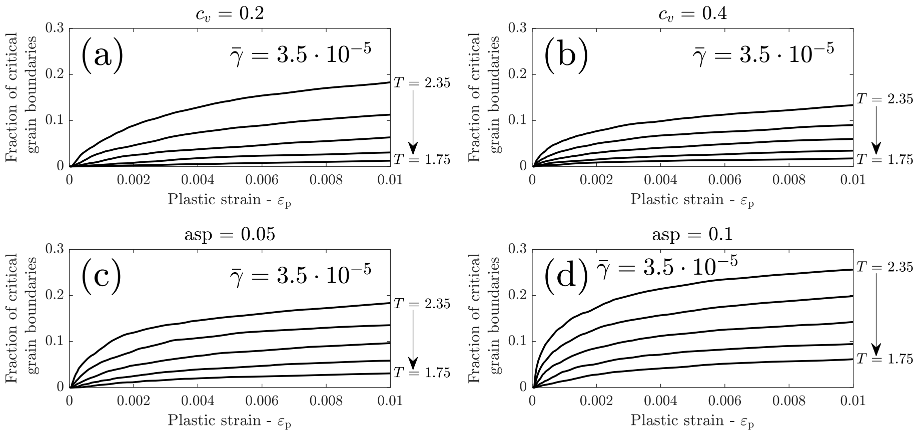

Fig. 10. The accumulated number fraction of critical grain boundaries in the models pertaining to (a) $c_v = 0.2$, (b) $c_v = 0.4$, (c) asp = 0.05, and (d) asp = 0.1. Each line represents a solution where the stress triaxiality T belongs to the set {2.35, 2.2, 2.05, 1.9, 1.75}.

the fraction of critical grain boundaries appears to accumulate with the same characteristic in all models. That is, no critical grain boundaries during initial elastic straining followed by a rapid increase which more or less stabilizes at increased plastic straining. The overall accumulated number of critical grain boundaries is directly dependent to the surface energy $\bar{\gamma}$. However, the characteristic of the accumulation of critical grain boundaries remains, to a large extent, the same for a reasonable range of $\bar{\gamma}$. The data plotted in Fig. 10 is considered to be proportional to the h_1-function of the weakest link model, i.e. the resulting g_1-function would need to be decreasing with respect to plastic strain. By choosing a form of g_1 that results in the following expression for h_1

$$h_1 = c \int_{\varepsilon^{\mathrm{p}}} \frac{1}{\varepsilon_0 \left(1 + \varepsilon^{\mathrm{p}}/\varepsilon_0\right)} \, \mathrm{d}\varepsilon^{\mathrm{p}}, \tag{30}$$

a least square fit of c and ε_0 with a resulting $R^2 = 0.99$ or better is achieved for all levels of triaxiality. Indicating that $g_1 = c/\left(\varepsilon_0\left(1 + \varepsilon^{\mathrm{p}}/\varepsilon_0\right)\right)$ is a good candidate for the grain boundary failure mechanism. This functional form was chosen since a logarithmic dependency between the accumulated number of critical grain boundaries and the plastic strain was observed from the analysis. The parameter ε_0 was introduced to avoid the singularity at zero and can be seen as a shape parameter for the logarithmic behavior of g_1, a smaller value will yield a sharper behavior and a larger value will yield a smoother behavior.

In Fig. 11 the average normal stress σ_{n} acting on each grain boundary in the equiaxed model is visualized, where the model with $c_v = 0.4$ has been used. The stress state is plotted at a global plastic strain $\varepsilon^{\mathrm{p}} = 0.005$. In Fig. 11(a), σ_{n} is plotted against the grain boundary misorientation θ, calculated according to Randle (1993). In Fig. 11(b), σ_{n} is plotted against the polar angle between the grain boundary normal and the normal of the global maximum principal stress acting over the RVE. Lastly, in Fig. 11(c), σ_{n} is plotted against the grain boundary area normalized with the mean grain boundary area. In Fig. 11(c), the Griffith criterion is also illustrated where grain boundaries exceeding the critical stress are colored red as opposed to the non critical which are colored black. This color coding applies to all subfigures. Clearly, the results in Fig. 11(b) shows that grain boundaries with a normal aligning with the maximum principal stress appears to be more prone to failure. The results in Fig. 11(a) are not as clear, i.e. no strong coupling between the failed grain boundaries and the grain boundary misorientation appears to be seen. The results for the other models considered are similar to the results shown in Fig. 11, which is why they are not shown here.

At this juncture, it is of interest to find out how the crystal microstructure influences the local normal stress at the grain boundaries in relation to the normal stress obtained from the global stress state corresponding to the grain boundary normal. This is shown in Fig. 12 where the average normal stress at each grain boundary is normalized by the normal stress obtained from the global stress state. This means, if the ratio $\sigma_{\mathrm{n}}/\Sigma_{\mathrm{N}}$ is unity, the grain boundary stress is fully controlled by the global stress state, while any deviation from unity indicates an influence of the crystal microstructure. From this figure, it can be observed that the ratio does not deviate much from unity in the vast majority of the grain boundaries in the model. If the variation around unity in Fig. 12 can be neglected, an analytical model for grain boundary failure may suffice. Such a model will be developed next.

4.3. Analytical model for grain boundary crack nucleation

Consider a volume akin to the models in Section 4.2 subjected to a stress state defined by T, L and σ_{e}. Then, the principal stresses can be expressed as

$$\sigma_{\mathrm{I}} = \sigma_{\mathrm{e}} \left(T + \frac{3 - L}{3\sqrt{L^2 + 3}} \right), \tag{31}$$

$$\sigma_{\mathrm{II}} = \sigma_{\mathrm{e}} \left(T + \frac{2L}{3\sqrt{L^2 + 3}} \right), \tag{32}$$

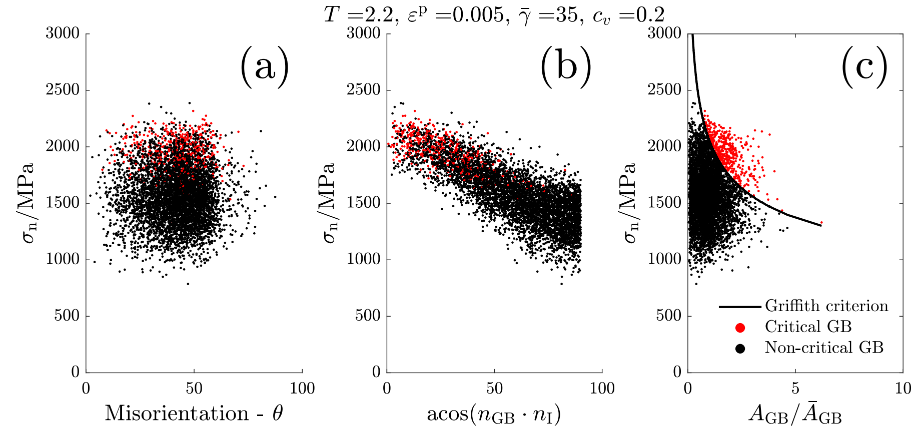

Fig. 11. Illustration of the grain boundary normal stress σ_{n} as a function of (a) grain boundary misorientation, (b) the polar angle in degrees from the maximum principal stress direction, and (c) the grain boundary area normalized by the mean grain boundary area, here is also the Griffith criterion illustrated. Note the color coding where red indicates a critical grain boundary and black indicates a non-critical grain boundary. (For interpretation of the references to colour in this figure legend, the reader is referred to the web version of this article.)

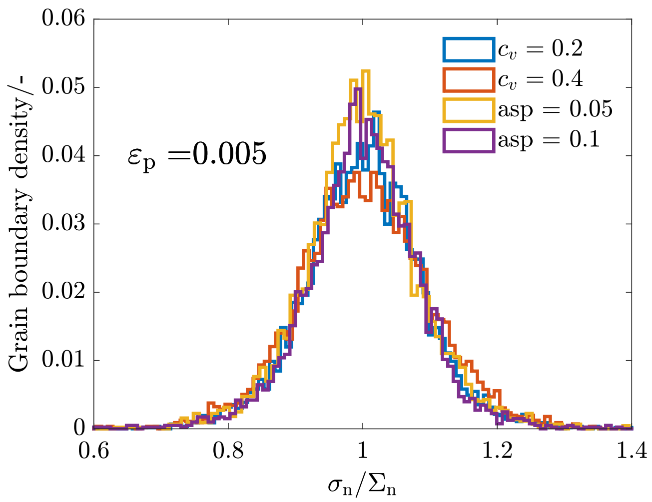

Fig. 12. Histogram of the distribution of the grain boundary stress normalized by the global stress (over RVE) projected on the grain boundary normal. In perfect isotropy, all bars would align at unity. The standard deviation of the datasets is σ_{GB} = {0.087, 0.097, 0.087, 0.084}, respectively for $c_v = 0.2$, $c_v = 0.4$, asp = 0.05 and asp = 0.1. (For interpretation of the references to colour in this figure legend, the reader is referred to the web version of this article.)

$$\sigma_{\mathrm{III}} = \sigma_{\mathrm{e}}\left(T - \frac{3+L}{3\sqrt{L^2+3}}\right). \tag{33}$$

The effective stress σ_{e} is specified as a flow strength relation on the form $\sigma_{\mathrm{e}} = \sigma_{\mathrm{ref}}\left(\varepsilon^{\mathrm{p}}/\varepsilon_{\mathrm{ref}}\right)^m$ where the plastic strain ε^{p} is used as a loading parameter. The parameters were estimated to yield an as-similar response as the crystal model as possible. The grain boundary areas are randomly drawn from a log-normal distribution (to emulate the same distribution as in the crystal models) and the normals are taken as uniformly distributed over the unit sphere. The critical stress of each grain boundary is calculated in the same manner as in the crystal models and the post processing regarding the accumulation of critical grain boundaries occurs in the same way.

Considering a case with 5000 grain boundaries and distribution parameters for the area distribution corresponding to the crystal models, the outcome seen in Fig. 13 results, which is compared to the outcome of the crystal models. It can be clearly seen that the results from the crystal model is reproduced by the analytical model. By using the analytical model to investigate a wider range of stress triaxialites the results in Fig. 14 are obtained. Interestingly, a threshold in the triaxiality below which no critical grain boundaries can be found appears to emerge. By inferring a g_1-function from these results, the following expression can be used to

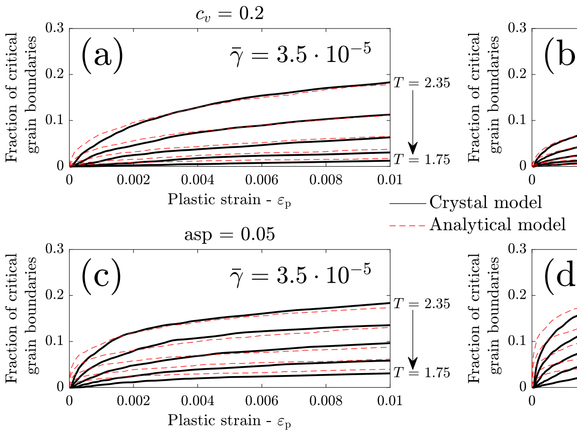

Fig. 13. Comparison of the accumulated number fraction of critical grain boundaries between analytical model and the crystal models pertaining to (a) $c_v = 0.2$, (b) $c_v = 0.4$, (c) asp = 0.05, and (d) asp = 0.1. Each line represents a solution where the stress triaxiality T belongs to the set {2.35, 2.2, 2.05, 1.9, 1.75}. (For interpretation of the references to colour in this figure legend, the reader is referred to the web version of this article.)

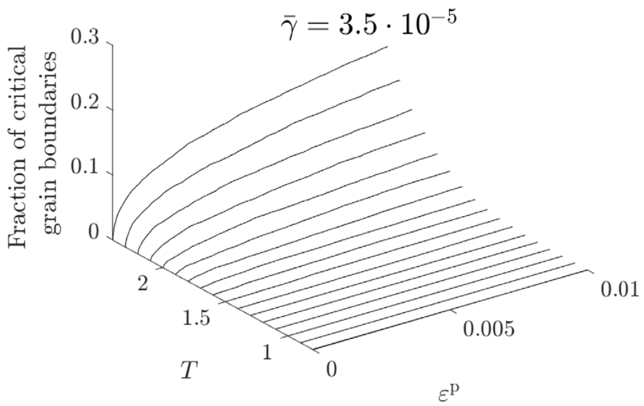

Fig. 14. The accumulated number fraction of critical grain boundaries calculated by the analytical model with the purpose of exploring the influence of the stress triaxiality. Note the threshold effect in the lower end of the triaxiality axis.

reproduce the behavior with a $R^2 = 0.996$

$$h_1 = \begin{cases} c \int_{\varepsilon^p} \frac{(T - T_{th})^2}{\varepsilon_0 (1 + \varepsilon^p / \varepsilon_0)} \, d\varepsilon^p & \text{for } T > T_{th}, \\ 0 & \text{for } T \leqslant T_{th}. \end{cases} \tag{34}$$

5. Application of probabilistic model to experiments

From the micro mechanical investigation in Section 4, two candidates for the g_1-function could be inferred for the grain boundary mechanism in the weakest link framework detailed in Section 3. This section presents the estimation of parameters and application to experiments of the micro mechanically informed weakest link model for multiple mechanism brittle fracture. The estimation of parameters was carried out by minimizing the residual $R = R_I + R_{II}$ using the Nelder–Mead simplex algorithm (Nelder and Mead, 1965), where superscript I and II relates to the high and low constraint experiments used in the estimation of model parameters. The partial residuals R_I and R_{II} were computed as

$$R_I = \sum_{i=1}^{N_I} [P^i_{rank} - P_f(J^i_c)]^2, \; R_{II} = \sum_{i=1}^{N_{II}} [P^i_{rank} - P_f(J^i_c)]^2. \tag{35}$$

For details regarding the calculations pertinent to the weakest link model, the reader is referred to Faleskog et al. (2004), Kroon et al. (2008) and Boåsen et al. (2019).

The length scales used to compute the non-local stress in (18) needs to be properly resolved over the mesh used in the FE-models. With the models used for the weakest link calculations, the length scales reaches over ~5 elements per element along the axis of

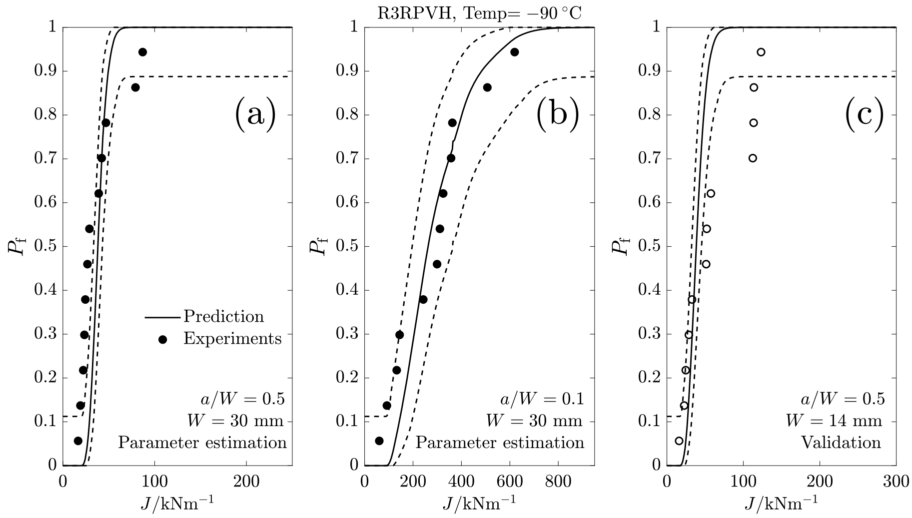

Fig. 15. Comparison of the predicted failure probability with rank probabilities for the fracture tests (circles) of the reference material R3RPVH data set tested at a temperature of −90 °C. (a) subset where $a/W = 0.5$ and $W = 30$ mm, (b) subset where $a/W = 0.1$ and $W = 30$ mm, and (c) subset where $a/W = 0.5$ and $W = 14$ mm. Subsets (a) and (b) were used for parameter estimation, subset (c) were used as validation of model predictions.

Table 4
Model parameters used in the weakest link model. (a) Single mechanism model for R3RPVH. (b) Multiple mechanism model for R4PRZ.

	Parameter	Value	Parameter	Value	Parameter	Value
(a)	$\frac{c/V_0}{10^{12}/\mathrm{m}^3}$	75.995	$\sigma_{\mathrm{th}}/\mathrm{MPa}$	2019.5	$L/\mu\mathrm{m}$	50.0
(b)	$\frac{c^{\mathrm{A}}/V_0}{10^{12}/\mathrm{m}^3}$	4.9254	$\sigma^{\mathrm{A}}_{\mathrm{th}}/\mathrm{MPa}$	1921.6	$L/\mu\mathrm{m}$	50.0
			$\sigma^{\mathrm{B}}_{\mathrm{th}}/\mathrm{MPa}$	1008.9	$L/\mu\mathrm{m}$	50.0
(36a)	$\frac{c^{\mathrm{B}}/V_0}{10^{6}/\mathrm{m}^3}$	6.1724	$\varepsilon_0/10^{-8}$	1.1		
(36b)	$\frac{c^{\mathrm{B}}/V_0}{10^{6}/\mathrm{m}^3}$	50.608	$\varepsilon_0/10^{-8}$	1.1	T_{th}	0.808

crack propagation in the fine mesh region. The length scales used can be found in Table 4 and an overview of the models used can be seen in Fig. 2.

Concerning the material used as a reference in this study, R3RPVH, the fracture toughness distribution appears to be unimodal. Also, the cleavage initiation mechanism in the reference material was traced back to second phase particles. Therefore, a single mechanism weakest link framework has been applied to the fracture tests of R3RPVH, i.e. a single, constant g_1-function was used as $g_1 = c$. The outcome of the parameter estimation and application of the model to the reference material, R3RPVH, can be seen in Fig. 15. It is clearly seen that a single mechanism weakest link framework including the effect of potential void formation, is capable of describing the fracture toughness distribution for the cases considered.

Regarding the aged material, R4PRZ, where two initiation mechanisms are able to initiate brittle fracture, i.e. grain boundaries and second phase particles, the multiple mechanism weakest link framework needs to be used. For the transgranular mechanism a constant $g_1^{\mathrm{A}} = c^{\mathrm{A}}$ was used just as for the reference material. Concerning the choice of g_1 for the grain boundary mechanism, the following two candidates have been found in Section 4 to describe the rate of critical grain boundaries per plastic strain

$$g_1 = c\frac{1}{\varepsilon_0\left(1+\varepsilon^{\mathrm{p}}/\varepsilon_0\right)}, \tag{36a}$$

$$g_1 = \begin{cases} c\,\frac{(T-T_{\mathrm{th}})^2}{\varepsilon_0(1+\varepsilon^{\mathrm{p}}/\varepsilon_0)} & \text{for } T > T_{\mathrm{th}}, \\ 0 & \text{for } T \leqslant T_{\mathrm{th}}. \end{cases} \tag{36b}$$

Here Eq. (36a) only depends on plastic strain and has two parameters to describe the rate of micro crack nucleation. Eq. (36b) depends of both plastic strain and the stress triaxiality and has three parameters, where two are the same as the previous case and the third is a threshold parameter in the stress triaxiality T_{th}. The importance of resolving the integral for the hazard function in (16) throughout the loading history should be noted. Especially for the grain boundary mechanism, even with 500 load steps in the FE-models, additional steps had to be added by linear interpolation of the pertinent fields before convergence was reached in the

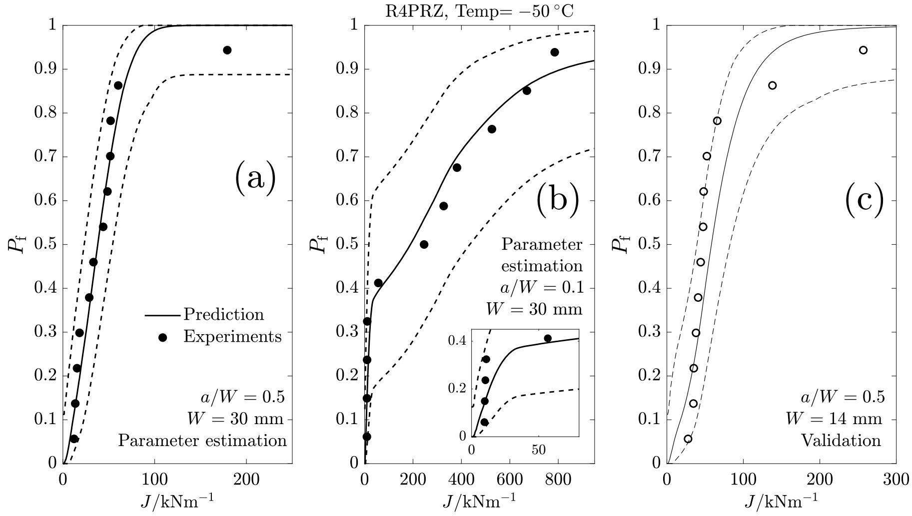

Fig. 16. Comparison of the predicted failure probability with rank probabilities for the fracture tests (circles) of the thermally aged R4PRZ data set tested at a temperature of −50 °C. (a) subset where $a/W = 0.5$ and $W = 30$ mm, (b) subset where $a/W = 0.1$ and $W = 30$ mm, and (c) subset where $a/W = 0.5$ and $W = 14$ mm. Subsets (a) and (b) were used for parameter estimation, subset (c) were used as validation of model predictions. Note, in (b) figure inset shows steep initial region of model prediction.

weakest link predictions. By considering both Eq. (36a) and (36b) the parameters pertinent to the weakest link model for multiple mechanisms can be estimated. The parameters of the model can be found in Table 4, note the normalization of the parameter c in Eq. (36a) and (36b). Interestingly, parameter estimates comes out the same with the exception of the parameter c in Eq. (36a) and (36b). It was found that the prediction of the fracture toughness distribution appears to be rather insensitive to the choice of g_1 with respect to the proposed functions in this study. The model predictions are shown together with the experimental fracture test results in Fig. 16, where (36a) was used. In Fig. 17 the model predictions together with the underlying mechanisms are illustrated, where each mechanism is calculated as if being the sole mechanism, i.e. by a single mechanism weakest link expression. It appears that the microstructurally informed weakest link model with multiple mechanisms for brittle fracture is able to describe the bimodal toughness distribution of the thermally aged material with a remarkable accuracy. Fig. 18 shows model predictions for SEN(B)-specimens with different sizes to illustrate the effect of size on the outcome of the model. It is clear that the intergranular fracture mechanism is subject to a distinct size effect where it may be suppressed in its entirety if the specimen size is small enough. On the other hand, if the specimen size is increased, the intergranular mechanism becomes more likely and will dominate given a large enough geometry.

6. Discussion and concluding remarks

The study presented in this paper is pertinent to modeling brittle failure of ferritic steels with multiple failure mechanisms. More specifically, aged low alloy steels in the case where the ageing introduces a second mechanism of brittle failure that alters the fracture toughness distribution from being unimodal to bimodal. In this paper it is shown how a multiple mechanism weakest link framework can be constructed to account for both intergranular and transgranular fracture. The mechanism for grain boundary controlled fracture has been inferred from crystal plastic simulations, which when introduced into the weakest link model, has been shown to be able to reproduce the fracture toughness distribution with a remarkable accuracy.

Regarding the crystal plastic models presented in Section 4, the modeling effort was carried out in order to motivate the choice of the g_1-function that governs the nucleation behavior of grain boundary micro cracks in the weakest link model. This was carried out by investigation of the grain boundary stress state which has been compared to a Griffith criterion for the critical stress. Another modeling approach for similar problems is using a cohesive zone methodology for the grain boundaries. This makes it possible to account for the local unloading due to the opening of a grain boundary crack, and its subsequent propagation in connecting grain boundaries. It was judged that such a sophisticated model would be overreaching for the cases in this study, on one hand, the investigation of the propagation would complicate the separation of nucleation and propagation. On another hand, the goal was to investigate the accumulation of grain boundaries that would be prone to nucleate micro cracks as function of the overall stress and strain state, where simplicity in the modeling effort was sought after. The Griffith criterion is normally used in analysis of crack propagation. Here it is regarded to represent the first barrier that needs to be overcome in the process that triggers the formation of a macroscopic brittle fracture, i.e. nucleation. It is here deemed that the transition from a micro crack to a self-sustaining macroscopic brittle crack is subject to dissipation on a higher level than that related to the nucleation of the micro crack itself.

From the results of accumulated number fraction of critical grain boundaries, the characteristic of the accumulation as function of plastic strain is the key result that is used in the choice of the g_1-function. The fact that all models appear to yield the same

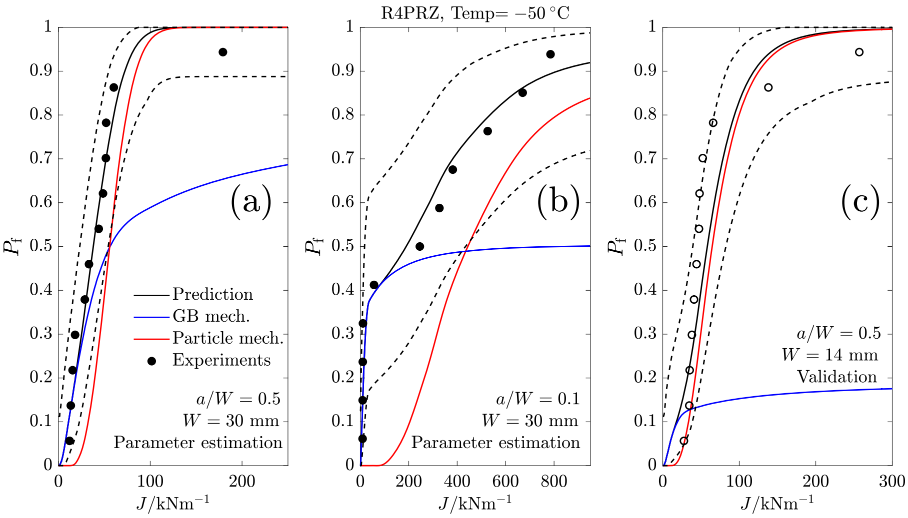

Fig. 17. Comparison of the predicted failure probability with rank probabilities for the fracture tests (circles) of the thermally aged R4PRZ data set tested at a temperature of −50 °C. Shown here is also the individual mechanisms calculated as if being single mechanism predictions. Note that the individual mechanisms as illustrated here does not sum up to the actual multi mechanism prediction since they are computed as single mechanism predictions and are for illustration purposes only. (For interpretation of the references to colour in this figure legend, the reader is referred to the web version of this article.)

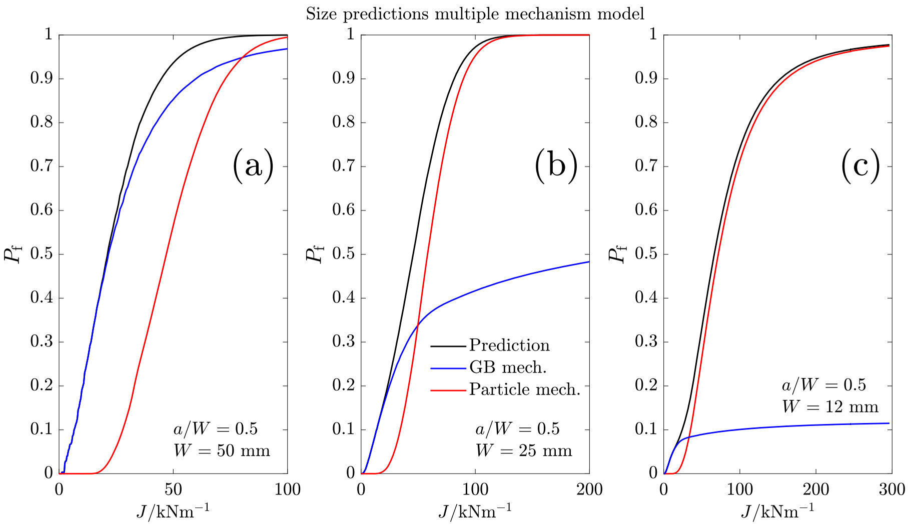

Fig. 18. Model predictions showcasing the size effect of the multiple mechanism weakest link model. Note that the intergranular mechanism is suppressed for the smaller geometry, and vice versa for the larger geometry. (a) Large specimen, W = 50 mm, (b) medium sized specimen, W = 25 mm, (c) small specimen, W = 12 mm. (For interpretation of the references to colour in this figure legend, the reader is referred to the web version of this article.)

characteristic stems from that the global stress state dictates the local grain boundary stress state, and also from the distribution of the grain boundary areas. Both act to make it possible to construct the analytical model presented in Section 4.3. The analytical model permits the investigation of a wider range of stress states, as the crystal models are very computational intensive and yields only one stress state per simulation.

In Section 2.2 of this paper, the modeling of fracture toughness tests using FE-models and a porous plastic constitutive model is presented. Even though by calibrating the model parameters at the higher temperature ductile tests at 75 °C, the model is able to predict the crack growth preceding the brittle fracture in the data sets at the temperatures −50 °C and −90 °C with satisfactory accuracy. Indicating that the model parameters of the porous plastic model is quite insensitive to temperature in this range. Regarding the void contribution from the strain controlled nucleation, which also controls the interplay between the ductile and brittle fracture in this framework, it is assumed to include the contribution from both mechanisms capable of participating in the brittle failure event. Second phase particles may either form a void due to particle cracking and subsequent crack arrest or by particle debonding and the grain boundaries may also form a void by cracking followed by crack arrest. This is why the void mechanism acts on both mechanisms in the final expression for the failure probability in Eq. (21). The parameter f_N could likely be divided in two parts, one for the contribution of second phase particles and one for grain boundaries. However, as these contributions would be small and close to inaccessible through physical measurements on the microstructure, it is deemed unnecessary and impractical to make such a division.

The reference material appears to be well described by a single mechanism weakest link framework, with the inclusion of the effect of the ductile mechanism. One key feature in the weakest link model developed by Kroon and Faleskog (2002) is the non-local stress, which is intended to account for the barriers that must be overcome by a microcrack (e.g. grain boundaries) before it develops into a self-sustaining macroscopic brittle fracture. In the estimation of parameters for the reference material and the aged material, the length scale that is used in the non-local integration is the same for both materials. Something which appears reasonable since the reference material should describe the aged material in an as manufactured state, having more or less the same microstructure and thereby barriers to propagation.

The weakest link model describes the fracture toughness distribution with a remarkable accuracy and is well fitted to two data sets used for parameter estimation. The fact that close to equal toughness predictions can be obtained with both g_1-functions presented in (36a) and (36b) is most likely due to that the range in stress triaxiality T is too narrow in the experiments presented here. This also indicates that solely relying on fracture test for calibrating the triaxiality threshold T_{th} might not he reliable. To elucidate the effect of the stress triaxiality more clearly, experiments with specimen sets pertaining to more distinct differences in T are deemed necessary. Thus for the predictions on fracture tests as presented here, the function $g_1 = c/\left(\varepsilon_0\left(1+\varepsilon^{\mathrm{p}}/\varepsilon_0\right)\right)$ is deemed sufficient in order to reduce the parameter space.

An interesting feature that emerges from the model is a significant size effect on the grain boundary mechanism such that the grain boundary mechanism could be suppressed in its entirety. This comes out in such a way that larger specimens will be more prone to result in grain boundary failure while smaller specimens might be close to or entirely without the mechanism. As is the case in this study, the grain boundary mechanism is more brittle than the particle mechanism, which indicates that fracture toughness testing on small specimens might be non-conservative, as the most brittle fracture mode might be obscured by the test method.

CRediT authorship contribution statement

Magnus Boåsen: Conceptualization, Methodology, Software, Validation, Formal analysis, Investigation, Resources, Data curation, Writing - original draft, Writing - review & editing, Visualization, Project Administration. **Carl F.O. Dahlberg:** Conceptualization, Methodology, Software, Writing - review & editing, Supervision. **Pål Efsing:** Conceptualization, Methodology, Writing - original draft, Writing - review & editing, Supervision, Funding acquisition, Project administration. **Jonas Faleskog:** Conceptualization, Methodology, Software, Formal analysis, Writing - original draft, Writing - review & editing, Supervision.

Declaration of competing interest

The authors declare that they have no known competing financial interests or personal relationships that could have appeared to influence the work reported in this paper.

Acknowledgments

The Swedish Radiation Safety Authority (SSM), Sweden and the Swedish Centre for Nuclear Technology (SKC), Sweden are acknowledged for their financial support. Ringhals AB is acknowledged for supplying the material that was used in the experimental investigation.

References

Anderson, T., 2005. Fracture Mechanics Fundamentals and Applications, third ed. Taylor & Francis.

ASTM, 2019a. Standard Test Method for Determination of Reference Temperature, T_0, for Ferritic Steels in the Transition Range. ASTM International, ASTM West Conshohocken, U.S., Geneva, Switzerland.

ASTM, 2019b. Standard Test Method for Measurement of Fracture Toughness. ASTM International, ASTM West Conshohocken, U.S., Geneva, Switzerland.

Barsoum, I., Faleskog, J., 2007. Rupture mechanisms in combined tension and shear —- Micromechanics. Int. J. Solids Struct. 44, 5471–5498. http://dx.doi.org/10.1016/j.ijsolstr.2006.09.031.

Beremin, F.M., Pineau, A., Mudry, J.C., D' Escatha, Y., Ledermann, P., 1983. A local criterion for cleavage fracture of a nuclear pressure vessel steel. Metall. Trans. A 14, 2277–2287. http://dx.doi.org/10.1007/BF02663302.

Boåsen, M., Lindgren, K., Öberg, M., Thuvander, M., Faleskog, J., Efsing, P., 2020. Analysis of Thermal Embrittlement of a Low Alloy Steel Weldment Using Fracture Toughness and Microstructural Investigations. Tech. rep., Solid Mechanics, Dept. of Engineering Mechanics, KTH.

Boåsen, M., Stec, M., Efsing, P., Faleskog, J., 2019. A generalized probabilistic model for cleavage fracture with a length scale – Influence of stress state and application to surface cracked experiments. Eng. Fract. Mech. 214, 590–608. http://dx.doi.org/10.1016/j.engfracmech.2019.03.041.

Bordet, S.R., Karstensen, A.D., Knowles, D.M., Wiesner, C.S., 2005a. A new statistical local criterion for cleavage fracture in steel. Part I: model presentation. Eng. Fract. Mech. 72, 435–452. http://dx.doi.org/10.1016/j.engfracmech.2004.02.009.

Bordet, S.R., Karstensen, A.D., Knowles, D.M., Wiesner, C.S., 2005b. A new statistical local criterion for cleavage fracture in steel. Part II: application to an offshore structural steel. Eng. Fract. Mech. 72, 453–474. http://dx.doi.org/10.1016/j.engfracmech.2004.02.010.

Briant, C.L., Banerji, S.K., 1978. Intergranular failure in steel: the role of grain boundary composition. Int. Met. Rev. 4, 164–199. http://dx.doi.org/10.1179/imtr.1978.23.1.164.

Chu, C.C., Needleman, A., 1980. Void nucleation effects in biaxially streched sheets. J. Eng. Mater. Technol. 102, 249–256. http://dx.doi.org/10.1115/1.3224807.

Dæhli, L.E.B., Børvik, T., Hopperstad, O.S., 2016. Influence of loading path on ductile fracture of tensile specimens made from aluminium alloys. Int. J. Solids Struct. 88–89, 17–34. http://dx.doi.org/10.1016/j.ijsolstr.2016.03.028.

Dæhli, L.E.B., Faleskog, J., Børvik, T., Hopperstad, O.S., 2017. Unit cell simulations and porous plasticity modelling for strongly anisotropic FCC metals. Eur. J. Mech. A Solids 65, 360–383. http://dx.doi.org/10.1016/j.euromechsol.2017.05.004.

Faleskog, J., Kroon, M., Öberg, H., 2004. A probabilistic model for cleavage fracture with a length scale —- parameter estimation and predictions of stationary crack experiments. Eng. Fract. Mech. 71, 57–79. http://dx.doi.org/10.1016/S0013-7944(03)00066-3.

Faleskog, J., Xiaosheng, G., Fong Shih, C., 1998. Cell model for nonlinear fracture analysis – I. Micromechanics calibration. Int. J. Fract. 89, 355–373. http://dx.doi.org/10.1023/A:1007421420901.

Gao, X., Faleskog, J., Fong Shih, C., 1998. Cell model for nonlinear fracture analysis - II. Fracture-process calibration and verification. Int. J. Fract. 89, 375–398. http://dx.doi.org/10.1023/A:1007410825313.

Griffith, A.A., 1921. The phenomena of rupture and flow in solids. Phil. Trans. R. Soc. A 221, 163–198. http://dx.doi.org/10.1098/rsta.1921.0006.

Gurland, J., 1972. Observations on the fracture of cementite particles in a spheriodized 1.05%C steel deformed at room temperature. Acta Metall. 20, 735–741. http://dx.doi.org/10.1016/0001-6160(72)90102-2.

Gurson, A.L., 1977. Continuum theory of ductile rupture by void nucleation and growth: Part I—Yield criteria and flow rules for porous ductile media. J. Eng. Mater. Technol. 99, 2–15. http://dx.doi.org/10.1115/1.3443401.

Hirth, J.P., Lothe, J., 1982. Theory of Dislocations, Vol. 1, second ed. Krieger publishing company, Appendix 1.

Hutchinson, J.W., 1976. Bounds and self-consistent estimates for creep of polycrystalline materials. Proc. R. Soc. Lond. A 348, 101–127. http://dx.doi.org/10.1098/rspa.1976.0027.

Kim, J., Xiaosheng, G., Tirumalai, S.S., 2004. Modeling of void growth in ductile solids: effects of stress triaxiality and initial porosity. Eng. Fract. Mech. 71, 379–400. http://dx.doi.org/10.1016/S0013-7944(03)00114-0.

Knott, J.F., 1977. Micro-mechanisms of fracture and the fracture toughness of engineering alloys. Int. J. Fract. 1, 61–82. http://dx.doi.org/10.1016/B978-0-08-022136-6.50016-0.

Kroon, M., Faleskog, J., 2002. A probabilistic model for cleavage fracture with a length scale – influence of material parameters and constraint. Int. J. Fract. 118, 99–118. http://dx.doi.org/10.1023/A:1022864513654.

Kroon, M., Faleskog, J., Öberg, H., 2008. A probabilistic model for cleavage fracture with a length scale — parameter estimation and predictions of growing crack experiments. Eng. Fract. Mech. 75, 2398–2417. http://dx.doi.org/10.1016/j.engfracmech.2007.08.009.

Lindley, T.C., Oates, G., Richards, C.E., 1970. A critical appraisal of carbide cracking mechanisms in ferrite/carbide aggregates. Acta Metall. 18, 1127–1136. http://dx.doi.org/10.1016/0001-6160(70)90103-3.

Liu, Z.G., Wong, W.H., Guo, T.F., 2016. Void behaviors from low to high triaxialities: Transition from void collapse to void coalescence. Int. J. Plast. 84, 183–202. http://dx.doi.org/10.1016/j.ijplas.2016.05.008.

McMahon, C.J., Cohen, M., 1965. Initiation of cleavage fracture in polycrystalline iron. Acta Metall. 13, 591–604. http://dx.doi.org/10.1016/0001-6160(65)90121-5.

Nahshon, K., Hutchinson, J.W., 2008. Modification of the Gurson model for shear failure. Eur. J. Mech. A Solids 27, 1–17. http://dx.doi.org/10.1016/j.euromechsol.2007.08.002.

Nanstad, R.K., Sokolov, M.A., Ortner, S.R., Styman, P.D., 2018. Neutron and Thermal Embrittlement of RPV Steels: An Overview. ASTM STP 1603, pp. 68–106. http://dx.doi.org/10.1520/STP160320170063.

Nelder, J.A., Mead, R., 1965. A simplex method for function minimization. Comput. J. 7, 308–313. http://dx.doi.org/10.1093/comjnl/7.4.308.

Newman, J.C.J., Raju, I.S., 1981. An empirical stress-intensity factor equation for the surface crack. Eng. Fract. Mech. 15, 185–192. http://dx.doi.org/10.1016/0013-7944(81)90116-8.

Nguyen, V.-D., Pardoen, T., Noels, L., 2020. A nonlocal approach of ductile failure incorporating void growth, internal necking, and shear dominated coalescence mechanisms. J. Mech. Phys. Solids 137 (103891), http://dx.doi.org/10.1016/j.jmps.2020.103891.

Nielsen, K.L., Tvergaard, V., 2010. Ductile shear failure or plug failure of spot welds modelled by modified Gurson model. Eng. Fract. Mech. 77, 1031–1047. http://dx.doi.org/10.1016/j.engfracmech.2010.02.031.

Quey, R., Dawson, P.R., Barbe, F., 2011. Large-scale 3D random polycrystals for finite element method: Generation, meshing and remeshing. Comput. Methods Appl. Mech. Engrg. 200, 1729–1745. http://dx.doi.org/10.1016/j.cma.2011.01.002.

Randle, V., 1993. The Measurement of Grain Boundary Geometry. Institute of Physics, Bristol.

Roters, F., Diehl, M., Shanthraj, P., Eisenlohr, P., Reuber, C., Wong, S.L., Maiti, T., Ebrahimi, A., Hochrainer, T., Fabritius, H.-O., Nikolov, S., Friak, M., Fujita, N., Grilli, N., Janssens, K.G.F., Jia, N., Kok, P.J.J., Ma, D., Meier, F., Werner, E., Stricker, M., Weygand, D., Raabe, D., 2019. DAMASK – the Düsseldorf advanced material simulation kit for modelling multi-physics crystal plasticity, damage, and thermal phenomena from the single crystal up to the component scale. Comput. Mater. Sci. 158, 420–478. http://dx.doi.org/10.1016/j.commatsci.2018.04.030.

Tvergaard, V., 1981. Influence of voids on shear band instabilities under plane strain conditions. Int. J. Fract. 17, 389–407. http://dx.doi.org/10.1007/BF00036191.

Tvergaard, V., 1982. Ductile fracture by cavity nucleation between larger voids. J. Mech. Phys. Solids 30, 265–286. http://dx.doi.org/10.1016/0022-5096(82)90033-3.

Tvergaard, V., Needleman, A., 1984. Analysis of the cup-cone fracture in a round tensile bar. Acta Metall. 32, 157–169. http://dx.doi.org/10.1016/0001-6160(84)90213-X.

Tvergaard, V., Needleman, A., 1995. Effects of nonlocal damage in porous plastic solids. Int. J. Solids Struct. 32, 1063–1077. http://dx.doi.org/10.1016/0020-7683(94)00185-Y.

Vadillo, G., Fernández-Sáez, J., 2009. An analysis of Gurson model with parameters dependent on triaxiality based on unitary cells. Eur. J. Mech. A Solids 28, 417–427. http://dx.doi.org/10.1016/j.euromechsol.2008.10.005.

Wallin, K., 1984. The scatter in K_{IC}-results. Eng. Fract. Mech. 19, 1084–1093. http://dx.doi.org/10.1016/0013-7944(84)90153-X.

Wallin, K., Nevasmaa, P., Laukkanen, A., Planman, T., 2004. Master curve analysis of inhomogeneous ferritic steels. Eng. Fract. Mech. 71, 2329–2346. http://dx.doi.org/10.1016/j.engfracmech.2004.01.010.

Was, G.S., 2007. Fundamentals of Radiation Materials Science: Metals and Alloys, Vol. 1, first ed. Springer Science & Business Media, Chapter 13.

Xia, L., Fong Shih, C., 1995. Ductile crack growth - I. A numerical study using computational cells with microstructurally-based length scales. J. Mech. Phys. Solids 43, 233–259. http://dx.doi.org/10.1016/0022-5096(94)00064-C.

Xia, L., Fong Shih, C., 1996. Ductile crack growth - III. Transition to cleavage fracture incorporating statistics. J. Mech. Phys. Solids 44, 603–639. http://dx.doi.org/10.1016/0022-5096(95)00086-0.

Yahya, O.M.L., Borit, F., Piques, R., Pineau, A., 1998. Statistical modelling of intergranular brittle fracture in low alloy steel. Fatigue Fract. Eng. Mater. Struct. 21, 1485–1502. http://dx.doi.org/10.1046/j.1460-2695.1998.00126.x.

Zienkiewicz, O.C., Taylor, R.L., 1991. The Finite Element Method, Vol. 2, fourth ed. McGraw-Hill Book Company, p. 266, Chapter 7, section 15.